ETH zürich

ETH Library

Three influential factors on colloidal nanoparticle deposition for heat conduction enhancement in 3D chip stacks

Journal Article

Author(s):
Qin, Feifei; Zhao, Jianlin; Kang, Qinjun; Brunschwiler, Thomas; Carmeliet, Jan; Derome, Dominique

Publication date:
2021-03-25

Permanent link:
https://doi.org/10.3929/ethz-b-000467215

Rights / license:
Creative Commons Attribution-NonCommercial-NoDerivatives 4.0 International

Originally published in:
Applied Thermal Engineering 187, https://doi.org/10.1016/j.applthermaleng.2021.116585

This page was generated automatically upon download from the ETH Zurich Research Collection.
For more information, please consult the Terms of use.

Applied Thermal Engineering 187 (2021) 116585

Contents lists available at ScienceDirect

Applied Thermal Engineering

journal homepage: www.elsevier.com/locate/apthermeng

Three influential factors on colloidal nanoparticle deposition for heat conduction enhancement in 3D chip stacks

Feifei Qin [a,b,*], Jianlin Zhao [a], Qinjun Kang [c], Thomas Brunschwiler [d], Jan Carmeliet [a], Dominique Derome [e]

[a] Chair of Building Physics, Department of Mechanical and Process Engineering, ETH Zürich (Swiss Federal Institute of Technology in Zürich), Zürich 8092, Switzerland
[b] Laboratory of Multiscale Studies in Building Physics, Empa (Swiss Federal Laboratories for Materials Science and Technology), Dübendorf 8600, Switzerland
[c] Earth and Environment Sciences Division (EES-16), Los Alamos National Laboratory (LANL), Los Alamos, NM 87545, USA
[d] Smart System Integration, IBM Research-Zürich, Saumerstrasse 4, 8803 Rüschlikon, Switzerland
[e] Dep. of Civil and Building Engineering, Université de Sherbrooke, Sherbrooke, Qc J1K 2R1, Canada

ARTICLE INFO

Keywords:
Nanoparticle concentration
Drying temperature
Surface wettability
Colloidal suspension
Heat conduction
3D chip stacks

ABSTRACT

Thermal management is one of the major challenges facing the development of three-dimensional (3D) chip stacks. Recently, experimental studies have shown that neck-based thermal structure (NTS) between chip layers formed by drying of colloidal suspension in cavity filled with micro-size particles can improve the vertical heat conduction threefold. However, a deep understanding of the mechanisms of neck formation and its influence on heat conduction is still lacking. In this paper, we numerically study the effects of three parameters, i.e., initial nanoparticle concentration, drying temperature and chip surface wettability on neck formation between filler particles and on the resulting heat conduction of the NTS. With increasing nanoparticle concentration, the size and number of necks increase, resulting in an increased effective thermal conductivity (ETC) of NTS. The drying temperature is found to have only little influence on the ETC of resultant NTS, while the neck size and spatial distribution become more uniform at higher drying temperature. When reducing the wettability of the top and bottom surfaces of the cavity, the necks shrink in size until completing evacuating at the top and bottom layers, while the size of the necks between filler particles in the middle height of the cavity expands slowly. In consequence, the ETC of NTS drops at an increasing rate. Being able to reveal the underlying multiple mechanisms of two-phase flow, phase change and heat transport, the current numerical study suggests optimal values for the deposition process, with initial nanoparticle concentration over 0.8%, a drying temperature of 60°C and a uniform contact angle of 30° for practical production of NTS.

Note: Only frequently used symbols are described here. All symbols below with physical units have corresponding lattice units in simulations.

1. Introduction

With the rapidly increasing demand of computational power, such as direct numerical simulation of fluid dynamics and deep learning algorithms, a much higher performance of computer chips is eagerly required. As a promising technique, the development of three-dimensional (3D) integrated chip stacks has become an active research area in last few decades [1–7]. In a 3D integrated chip stack, two or more layers of active electronic components are integrated vertically, as illustrated in Fig. S1 in Supplementary Materials. Compared to conventional spreading 2D chip design resulting in possible delay in power/signal delivery between different components, this 3D chip integration avoids the interconnect delay problems while saving energy by having short vertical interconnects with “through silicon via” (TSV) replacing the wire connections used in 2D chip designs [7,8]. Moreover, the increased integration density reduces the chip area, making a smaller chip size possible. Another improvement is the co-integration of heterogeneous components, which can combine various functions more conveniently: logic, memory, MEMS and RF are examples of these as shown in Fig. S1 in Supplementary Materials [9]. Therefore, 3D integration can significantly improve the performance of the overall system involving all functional components. Despite these promising

* Corresponding author at: Chair of Building Physics, Department of Mechanical and Process Engineering, ETH Zürich (Swiss Federal Institute of Technology in Zürich), Zürich 8092, Switzerland.
E-mail address: fqin@ethz.ch (F. Qin).

https://doi.org/10.1016/j.applthermaleng.2021.116585
Received 22 April 2020; Received in revised form 12 December 2020; Accepted 8 January 2021
Available online 13 January 2021
1359-4311/© 2021 The Author(s). Published by Elsevier Ltd. This is an open access article under the CC BY-NC-ND license (http://creativecommons.org/licenses/by-nc-nd/4.0/).

Nomenclature

Symbols	Terms (Units)
CA_{fp}	contact angle of filler particle (°)
$CA_{t,b}$	contact angle of top cover and bottom substrate (°)
d^a_{fp}, d^a_{neck}	average filler particle, neck diameter (μm)
$\widetilde{d}^a_{neck}, \widetilde{d}^t_{neck}$	normalized average, total neck diameter (–)
p	pressure (Pa)
q	heat flux (W/m^2)
$\widetilde{q}^t$	normalized total heat flux in a certain region (–)
r_1, r_2	curvature radii of pores in different directions (μm)
T, T_{top}, T_{bot}	temperature, temperature of top cover, bottom substrate (°C/K)
T_c, T_d, T_{en}	critical, drying, environment temperature (°C/K)
V_{cv}	volume of cavity between two chip layers (μm^3)
V^a_{fp}, V^a_{neck}	average filler particle, neck volume (μm^3)
$V^t_{fp}, V^t_{neck}, V^t_{np}$	total filler particle, neck, deposited nanoparticle volume (μm^3)
$\widetilde{V}^a_{neck}$	normalized average neck volume (–)
$\widetilde{V}^t_{fp}, \widetilde{V}^t_{neck}, \widetilde{V}^t_{np}$	normalized total filler particle, neck, deposited nanoparticle volume (–)
$\lambda(\lambda_{eff}$, ETC)	(effective) thermal conductivity (W/mK)
$\rho(\rho_l, \rho_v)$	density (liquid, vapor) (kg/m^3)
σ	surface tension (N/m)
ϕ_{np}	initial concentration of nanoparticles (–)
FPC	filler particle configuration (–)
LBM	lattice Boltzmann model (–)
NTS, PTS	neck-based, percolating thermal structure (–)

advantages, 3D integration is still confronted with critical challenges before it can be successfully applied in industry, such as design challenges, overheads induced by TSV, crosstalk between different layers and thermal issues [4,9]. Heat removal is a major challenge for 3D chip stacks due to the high power density of the 3D integration and the low thermal conduction between the different layers. This paper focuses on the thermal issues and potential alleviation strategies for enhancing heat transport.

Heat removal can occur through gas, liquid or solid phases. Backside air cooling is typically used in industrial applications [10–12]. However, although air cooling is cost-effective and reliably manageable, the maximum allowable heat dissipation is limited and not applicable for 3D chip stacks. Given that the heat transfer coefficient for liquid flow is much higher than the one for air flow, on-chip liquid cooling has been proposed to replace air cooling [13–17]. However, the on-chip microfluidic cooling exhibits several severe limitations in terms of reliability concerns, such as damages to the semiconductor chip due to high liquid pressure drop and temperature non-uniformity on the chip along the flow direction [18]. An alternative approach is to use flow boiling to convert the heat generated from chips to latent heat by liquid vaporization [19–22]. With such two-phase flow boiling, a reduced fluid flow rate is required leading to a smaller pressure drop, which can diminish the temperature non-uniformity at the chip surface [23]. Flow boiling can cause instability, i.e. the liquid–vapor interface may oscillate back and forth between the channel inlet and outlet [24]. Liquid and flow boiling on-chip cooling share the risks of using a liquid as coolant. For instance, liquid leakage can cause shortcut of the electronic elements. In addition, the fluid channels between the chip layers occupy a lot of space, making it difficult to form an effective bonding between different chip layers with sufficient mechanical strength. A resultant lack of mechanical strength may cause failure of the whole system. With heat removal using gas or liquid being non-satisfactory, heat removal by conduction in solids remains a strong option.

In the last few years, percolating thermal structures (PTSs) and neck-based thermal structures (NTSs) between vertical chip layers have been proposed to improve heat conduction in 3D chip stacks [25–29]. PTSs and NTSs are reported experimentally to increase heat conduction two- to threefold, compared to state-of-the-art capillary thermal structures (CTSs) [27]. NTS is the structure that retains the interest of this paper due to its relatively higher heat removal performance. The fabrication process of NTS in 3D chip stacks consists overall in 4 main steps, including centrifugation of filler particles between two chip layers, injection and evaporation of colloidal nanosuspension for neck formation, injection of viscous matrix material (epoxy, for instance) by capillary action and final curing of matrix material. The main fabrication steps are illustrated in Fig. 1, and more details can be found in [27]. The NTS does not bear the disadvantages of single- or two-phase cooling, such as liquid leakage, pressure drop or instability problem. Moreover, NTS shows a high mechanical strength with the adhesive bonding of the matrix material [27]. Therefore, NTS has a high potential to be applied in

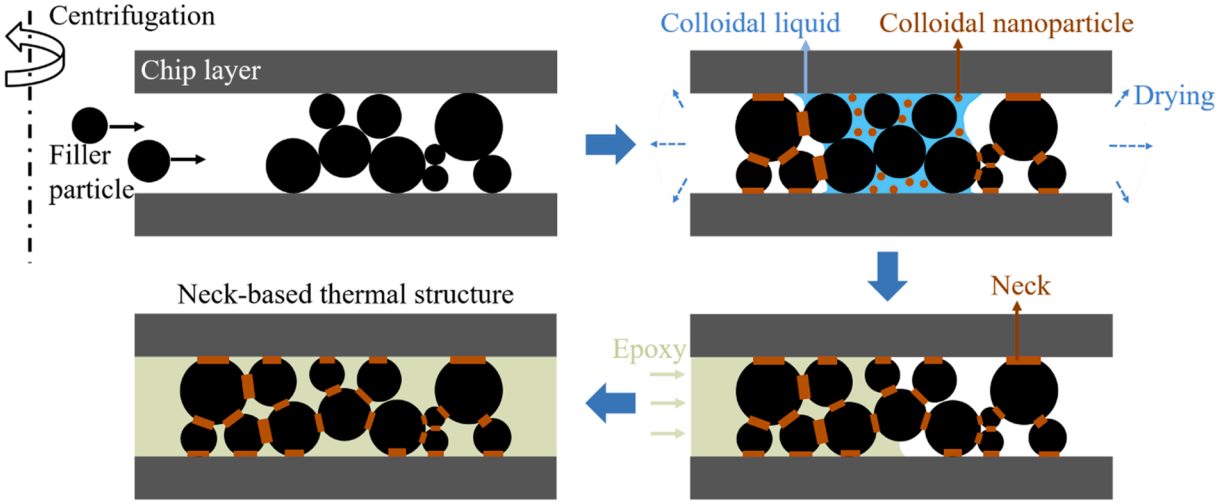

Fig. 1. Illustration of the main fabrication steps of neck-based thermal structure.

fabrication of 3D chip stacks. Although the thermal performance of NTS has been investigated experimentally [25–29], an in-depth understanding of the mechanisms of neck formation and its influence on heat conduction of NTS is still lacking and needs to be explored more systematically. As a powerful numerical approach, the lattice Boltzmann method (LBM) has been applied to study complex multi-phase [30–33], thermal [34–37] and particulate flows [38–41], as well as flow in porous media [42–44]. In our recent work [57], we have applied a tricoupled hybrid LBM [39,40] to study the drying of colloidal suspension in cavities with micro-size filler particles to form necks and thus to produce the NTS, and further evaluate the thermal performance of the NTS with a thermal LBM [45–47]. The modeling results are validated with experimental results from [27] in terms of neck size and effective thermal conductivity (ETC) of the NTS, in three different filler particle configurations of very similar filler particle volume fraction. However, we note that these processes can be influenced by the properties of liquid and nanoparticles [48–52], the drying temperature or temperature gradient [53,54], and drying conditions like air convection [55,56]. Furthermore, the neck formation influences the thermal performance of the resultant NTS. Therefore, a parametric study of the influential factors on neck formation and resultant thermal performances of NTS is eagerly demanded to assist the engineering design and production of NTS.

In this paper, with the validated tricoupled hybrid LBM and thermal LBM [39,45,46,57,58], we study the influences of three parameters on neck formation as well as the thermal performance of resultant NTS, including initial nanoparticle concentration, drying temperature and surface wettability of the chip layer. The mechanisms occurring during the studied processes are analyzed accordingly. The arrangement of the paper is as follows: the numerical models and validations are first given in Section 2, then the influences of initial nanoparticle concentration, drying temperature and chip surface wettability are analyzed in Sections 3, 4 and 5 respectively, while Section 6 concludes the present work with practical suggestions for the NTS production.

2. Numerical models

In this section, we briefly introduce the numerical models, i.e. a tricoupled hybrid LBM and a thermal LBM, for studying colloidal nanoparticle deposition as well as heat conduction in this paper. Afterwards, these models are validated for nanoparticle deposition in a micro-porous structure and evaluation of ETC in resultant NTS. For more detailed information on these models, the reader is referred to [30,34,39,45,58].

2.1. Tricoupled hybrid LBM

The tricoupled hybrid LBM is developed for simulating non-isothermal drying of colloidal suspension capable of dealing with different liquid properties, nanoparticle concentration, drying temperature, surface wettability and porous medium geometry [39,40,58]. This model consists of three sub-models, i.e. a pseudopotential LBM for isothermal two-phase flow [30], an extended temperature equation for heat convection/conduction and latent heat [34], and a modified convection diffusion equation for particle transport and deposition [39]. The sub-models and their coupling are introduced as following.

2.1.1. Isothermal two-phase pseudopotential LBM

When considering two-phase flow under isothermal condition, a pseudopotential LBM can be used with the following form:

$$f_i(\boldsymbol{x}+\boldsymbol{v}_i\delta t, t+\delta t) = f_i^{'} \equiv (1-\beta)f_i(\boldsymbol{x},t) + \beta f_i^{mirr}(\boldsymbol{x},t) + F_i, \tag{1}$$

where $\boldsymbol{x}$ is the location vector, t the time, δt the time step, $\boldsymbol{v}_i, i = 1,\ldots,Q$ the discrete velocities. f_i^{eq} is the equilibrium density population obtained by maximizing the entropy $S[f] = -\sum_{i=1}^{Q} f_i ln\left(\frac{f_i}{W_i}\right)$ under fixed density and momentum $\rho = \sum_{i=1}^{Q} f_i^{eq}, \rho\boldsymbol{u} = \sum_{i=1}^{Q} \boldsymbol{v}_i f_i^{eq}$ while W_i are the lattice weights. β is a free parameter to adjust the fluid kinematic viscosity ν by $\nu = c_s^2\left(\frac{1}{2\beta} - \frac{1}{2}\right)$, where $c_s = \delta x/(\sqrt{3}\delta t)$ is the lattice speed of sound. For standard LBM, $\delta x = \delta t = 1$ are used with a lattice speed of $c = 1$. f_i^{mirr} is the mirror state population constructed from the entropy maximization of the summarized post-collision population $f_i^{'}$ at each lattice site and time step, by properly relaxing high-order moments [30].

$F_i = f_i^{eq}(\rho, \boldsymbol{u}+\Delta\boldsymbol{u}) - f_i^{eq}(\rho,\boldsymbol{u})$ in equation (1) is an external force term which incorporates the fluid–fluid cohesive force $\boldsymbol{F}_c$ for phase separation and fluid–solid adhesive force $\boldsymbol{F}_w$ for realizing various wettability. The velocity increment is $\Delta\boldsymbol{u} = \boldsymbol{F}\delta t/\rho$ with the total force $\boldsymbol{F} = \boldsymbol{F}_c + \boldsymbol{F}_w$. With this force scheme, the real velocity of the two-phase fluid is $\boldsymbol{u}_f = \boldsymbol{u} + \Delta\boldsymbol{u}/2$. The expression of the fluid–fluid cohesive force is [59]:

$$\boldsymbol{F}_c = -\psi(\boldsymbol{x})\sum_{i=1}^{Q} w\left(|\boldsymbol{v}_i|^2\right)\left[G_1\psi(\boldsymbol{x}+\boldsymbol{v}_i) + G_2\psi(\boldsymbol{x}+2\boldsymbol{v}_i)\right]\boldsymbol{v}_i, \tag{2}$$

where the interaction potential is $\psi = \sqrt{2\left(P_{EoS} - \rho c_s^2\right)/(G_1+2G_2)c^2}$ and G_1, G_2 are the tuning coefficients for realizing different surface tensions σ independent of temperature ratio [30]. P_{EoS} is the equation of state (EoS), and here we adopt the Carnahan-Starling EoS [60]. $w(|\boldsymbol{v}_i|^2)$ are the force weights, which are used in both $\boldsymbol{F}_c$ and $\boldsymbol{F}_w$. The fluid–solid adhesive force $\boldsymbol{F}_w$ is represented as:

$$\boldsymbol{F}_w = -\psi(\boldsymbol{x})\sum_{i=1}^{Q} w\left(|\boldsymbol{v}_i|^2\right)\left[G_1\psi(\rho_w)I(\boldsymbol{x}+\boldsymbol{v}_i) + G_2\psi(\rho_w)I(\boldsymbol{x}+2\boldsymbol{v}_i)\right]\boldsymbol{v}_i, \tag{3}$$

where I is the indicator function that equals unity at solid nodes and zero at fluid nodes and ρ_w is the parameter to determine surface wettability. By varying ρ_w from liquid density ρ_l to vapor density ρ_v, different values of contact angle from around 0° to 180° can be realized [30].

2.1.2. Extended temperature equation

When dealing with non-isothermal liquid evaporation, heat convection/diffusion and latent heat for phase change should be considered. Based on local balance law of entropy and neglecting the viscous heat dissipation, the extended temperature equation is written as [61]:

$$\partial_t T = -\boldsymbol{u}_f\cdot\nabla T + \frac{1}{\rho c_V}\nabla\cdot(\lambda\nabla T) - \frac{T}{\rho c_V}\left(\frac{\partial P_{EOS}}{\partial T}\right)_\rho \nabla\cdot\boldsymbol{u}_f \tag{4}$$

where T, ρ, λ, c_V are the fluid temperature, density, thermal conductivity and specific heat capacity at constant volume, respectively. The three terms on the right-hand side represent heat convection, conduction and latent heat, respectively. This equation is solved with the finite difference method using a second-order Runge-Kutta scheme [34]. The coupling of two-phase pseudopotential LBM and extended temperature equation is two-way, i.e. at each iteration, the flow variables of density, velocity and pressure computed from the pseudopotential LBM are first used in the extended temperature equation for updating the temperature, then the updated temperature is inserted into the EoS to prepare for computing the flow variables by the pseudopotential LBM in the next iteration.

2.1.3. Modified convection diffusion equation

The coupling of two-phase pseudopotential LBM and extended temperature equation described above allows to study non-isothermal liquid drying. To further model drying of colloidal suspension, the transport and deposition of nanoparticles have to be considered. Here we apply a Eulerian model to represent the nanoparticle as a solute, and the governing equation is [39]:

$$\frac{\partial\phi}{\partial t} + \nabla\cdot(\phi\boldsymbol{u}_p) = \nabla\cdot(D_p\nabla\phi), \tag{5}$$

where ϕ represents the nanoparticle concentration, and $\boldsymbol{u}_p$ is the nanoparticle transport velocity modified as $\boldsymbol{u}_p = \boldsymbol{u}_{f,m} + \Delta\boldsymbol{u}_p$ from the fluid velocity. We use $\boldsymbol{u}_{f,m} = \boldsymbol{u}_f$ in liquid, where $\boldsymbol{u}_f$ is the liquid velocity obtained in two-phase LBM and $\boldsymbol{u}_{f,m} = 0$ in vapor since nanoparticles can only be present within the liquid phase. The velocity increment $\Delta\boldsymbol{u}_p = \boldsymbol{F}_p\delta t/\rho_p$ models the fluid-particle interaction $\boldsymbol{F}_p$ described as:

$$\boldsymbol{F}_p = -\phi\cdot\psi(\rho_p)\sum_{i=1}^{Q} w(|\boldsymbol{v}_i|^2)[G_1\psi'(\boldsymbol{x}+\boldsymbol{v}_i) + G_2\psi'(\boldsymbol{x}+2\boldsymbol{v}_i)]\boldsymbol{v}_i, \tag{6}$$

where ψ' is a modified potential of ψ from equation (2) [39]. In this way, the nanoparticle velocity $\boldsymbol{u}_p$ can represent both its convective motion in the liquid and accumulation around the liquid–vapor interface during drying. The diffusion in liquid phase is described by the right-hand side term of equation where D_p is the diffusion coefficient derived from the Stokes-Einstein equation [39]. In the experiments [27] and our current simulations, the estimated Peclet number of nanoparticles is $Pe_{np} = \overline{U}H/D_p \sim 10^2$ [57], where $\overline{U}$, H are the characteristic velocity of liquid flow and cavity height between chip layers, respectively. The high Pe_{np} indicates that the nanoparticle diffusion time scale is much longer than the convective time scale due to liquid capillary flow induced by drying. Therefore, the nanoparticle transport time scale is basically the same as the liquid drying time scale. Nanoparticle deposition occurs when the local concentration reaches 1.0 and it is adjacent to a solid surface or another deposition. To conserve the nanoparticle mass, a zero-flux boundary condition is applied at the solid boundary. More details of the boundary conditions are referred to [39,57]. We note that the nanoparticle surface wettability is not considered by assuming nanoparticle to be always fully immersed in the liquid phase. Similar to the extended temperature equation, equation is also solved by a second-order Runge-Kutta scheme.

The coupling between non-isothermal two-phase flow and nanoparticle transport and deposition is also two-way, i.e. the nanoparticle velocity is modified from the fluid velocity while the deposited nanoparticles can affect the fluid flow.

2.2. Thermal LBM

We apply a thermal LBM here to solve the heat conduction equation for temperature and heat flux distribution in NTS, and further evaluate the ETC of NTS. The heat conduction equation with no phase change and no convection is written as [45]:

$$(\rho c_p)_{ps}\frac{\partial T}{\partial t} = \lambda_{ps}\nabla^2 T \tag{7}$$

where the subscript ps represents different phases or components, which are filler particles, nanoparticle necks and epoxy in this paper. The other parameters ρ, c_p, T, t and λ are density, specific heat capacity, temperature, time and thermal conductivity, respectively. Equation (7) is solved by the following thermal LBM neglecting the thermal contact resistance of different phases or components at their interfaces [46]:

$$g_i(\boldsymbol{x}+\boldsymbol{v}_i\delta t, t+\delta t) - g_i(\boldsymbol{x},t) = -\frac{1}{\tau_{ps}}[g_i(\boldsymbol{x},t) - g_i^{eq}(\boldsymbol{x},t)] \tag{8}$$

where g_i^{eq} is the equilibrium form of temperature distribution and τ_{ps} is the relaxation time. Here we use a three-dimensional fifteen-velocity (D3Q15) LBM where [46]

$$\tau_{ps} = \frac{9}{5}\frac{\lambda_{ps}}{(\rho c_p)_{ps}c_{s,s}^2\delta t} + 0.5 \tag{9}$$

and $c_{s,s}$ is a pseudo sound speed whose value can take any positive value theoretically only to ensure the value of τ_{ps} within (0.5, 2) [45]. In this way, the temperature T and heat flux q can be solved as:

$$\begin{cases} T = \sum_i g_i \\ q = (\rho c_p)_{ps}\left(\sum_i \boldsymbol{v}_i g_i\right)\dfrac{\tau_{ps}-0.5}{\tau_{ps}}. \end{cases} \tag{10}$$

Moreover, the ETC (λ_{eff}) can be evaluated by the following equation:

$$\lambda_{eff} = \frac{L\int q dA}{\Delta T\int dA}, \tag{11}$$

where q is the steady state heat flux through the cross section dA with a temperature difference ΔT over the distance of L. We note that we only use the steady state version of equation (7) to determine the effective thermal conductivity.

2.3. Model validations

The tricoupled LBM has been validated by comparison of nanoparticle deposition after drying of colloidal suspension with experimental results in different micro-porous structures [39,58]. The thermal LBM has also been validated by evaluating ETC in different composite structures [45,46,62]. We have further validated these models considering the micro-porous structure of our 3D chip stack with details shown in [57]. Here we give a brief overview of the validations considering the colloidal nanoparticle deposited neck structure and ETC of the resultant NTS in [57].

2.3.1. Neck formation by colloidal nanoparticle deposition

As illustrated in Fig. 1, the filler particle configuration (FPC) is first obtained in the experiment by centrifugation of micro-sized filler particles into the cavity between two chip layers [27]. In our modeling, the FPC is realized using the discrete element method LIGGGHTS 3.3.1. Our FPC size is about $240 \times 240 \times 60$ μm^3 including 82 filler particles with the diameter of 34 ± 2 μm, resulting in a filler particle volume fraction of around 48.8%, as shown in Fig. 2a. Specifically, the FPC has 9, 23, 21, 21 and 8 (for a total of 82) filler particles with diameter of 32, 33, 34, 35 and 36μm, respectively. The filler particle volume fraction is defined as $\widetilde{V}_{fp}^t = V_{fp}^t/V_{cv}$ where V_{fp}^t and V_{cv} represent the total filler particle volume and cavity volume, respectively. The contact angle of all the surfaces, i.e. the two chip layers and the micro-sized filler particles is 30° in this simulation. Due to the limitation of computational resources, this system is small compared to the actual chip size [27], but similar relative filler particle volume fraction (48.8% in simulation and 47% in experiment) and filler particle size (34 ± 2 μm) ensure that the simulation domain is employed as an appropriate unit volume element.

Afterwards, an alumina nanoparticle (spherical) suspension with a concentration of $\phi_{np} = 3.7\%$ is injected into the FPC for evaporation under a heating temperature of 60 °C (333.15 K) [27]. The colloidal liquid is deionized water. At the drying temperature 60 °C, the density, dynamic viscosity, surface tension, thermal conductivity and specific heat capacity are 983 kg/m^3, 0.066 N/m, 4.66×10^{-4} N·s/m^2, 0.65 W/mK and 4.17 kJ/kgK, respectively. In current study, we do not consider the effect of nanoparticle concentration on colloidal liquid properties. With a room temperature of 25 °C (298.15 K), the temperature difference between the heating temperature and the environment is 35 K. With the water critical temperature (T_c) of 647 K, the ratio of the temperature difference to the critical temperature becomes $35/647 \approx 5.5\%$. In the current simulation, the setup shown in Fig. 2a is to represent the drying condition in the experiment aforementioned. We use $T_{eq} = 0.75T_c$ with a density ratio of $\rho_l/\rho_g \approx 30$ to represent isothermal conditions (25 °C), due to the limitation of our current LBM model in simulating the real density ratio of around 1000, which would require $T = 0.46T_c$. The drying temperature T_d in simulations is obtained by ensuing the same relative temperature difference as in

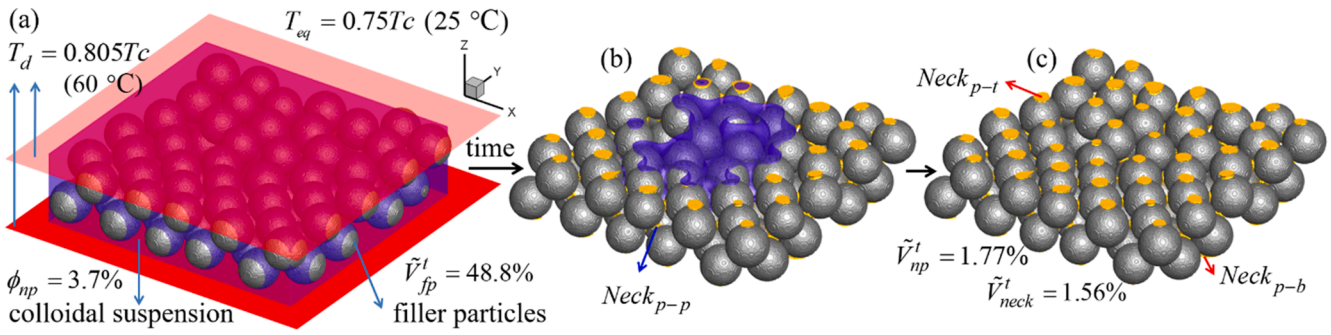

Fig. 2. Neck formation by drying of colloidal suspension with the initial nanoparticle concentration $\phi_{np} = 3.7\%$. (a) Simulation setup. (b) Intermediate state during the drying process (full drying process in Supplementary movie 1). (c) Final neck formation after drying completed.

experiment, i.e. $d\tilde{T} = (T_d - T_{eq})/T_c$. Thus, the drying temperature is set as $T_d = (0.75 + 0.055)T_c = 0.805T_c$ for the whole system, including the top cover, bottom substrate, colloidal suspension and filler particles, to be compatible with the experiment. The equilibrium temperature $T_{eq} = 0.75T_c$ is considered as the environment temperature (25 °C) at the boundaries of the four lateral sides. The contact angle of all the surfaces, i.e. the two chip layers and the micro-sized filler particles is 30° in this simulation.

Fig. 2b illustrates an intermediate state during the drying process and Fig. 2c shows the final neck formation after complete drying with initial concentration $\phi_{np} = 3.7\%$. From Fig. 2c we can see that the necks only form at the locations with smallest curvature radius, i.e. the gap between adjacent filler particles ($Neck_{p-p}$), between filler particle and top cover ($Neck_{p-t}$), and between filler particle and bottom substrate ($Neck_{p-b}$), which are the same as observed in the experiment [27]. To quantitatively validate the model, we compare the simulated neck size with experimental results. In the experiment of [27], the normalized average neck size at the top and bottom $\tilde{d}^a_{neck}(Neck_{p-t,p-b}) = d^a_{neck}(Neck_{p-t,p-b})/d^a_{fp}(Neck_{p-t,p-b})$, i.e. the ratio of average neck diameter and average filler particle diameter at the top and bottom is measured to be around 40%. In current simulation, it is calculated as 39.4%, which is very close to the experimental result. To test the dependence of our results on geometry, we have done simulations with three different FPCs with similar filler particle volume fraction $\tilde{V}^t_{fp} = 48.8\%, 48.0\%, 47.1\%$ in [57], and the resultant $\tilde{d}^a_{neck}(Neck_{p-t,p-b}) = 39.4\%, 41.7\%, 42.2\%$ are very close, indicating a high accuracy of the tricoupled hybrid LBM.

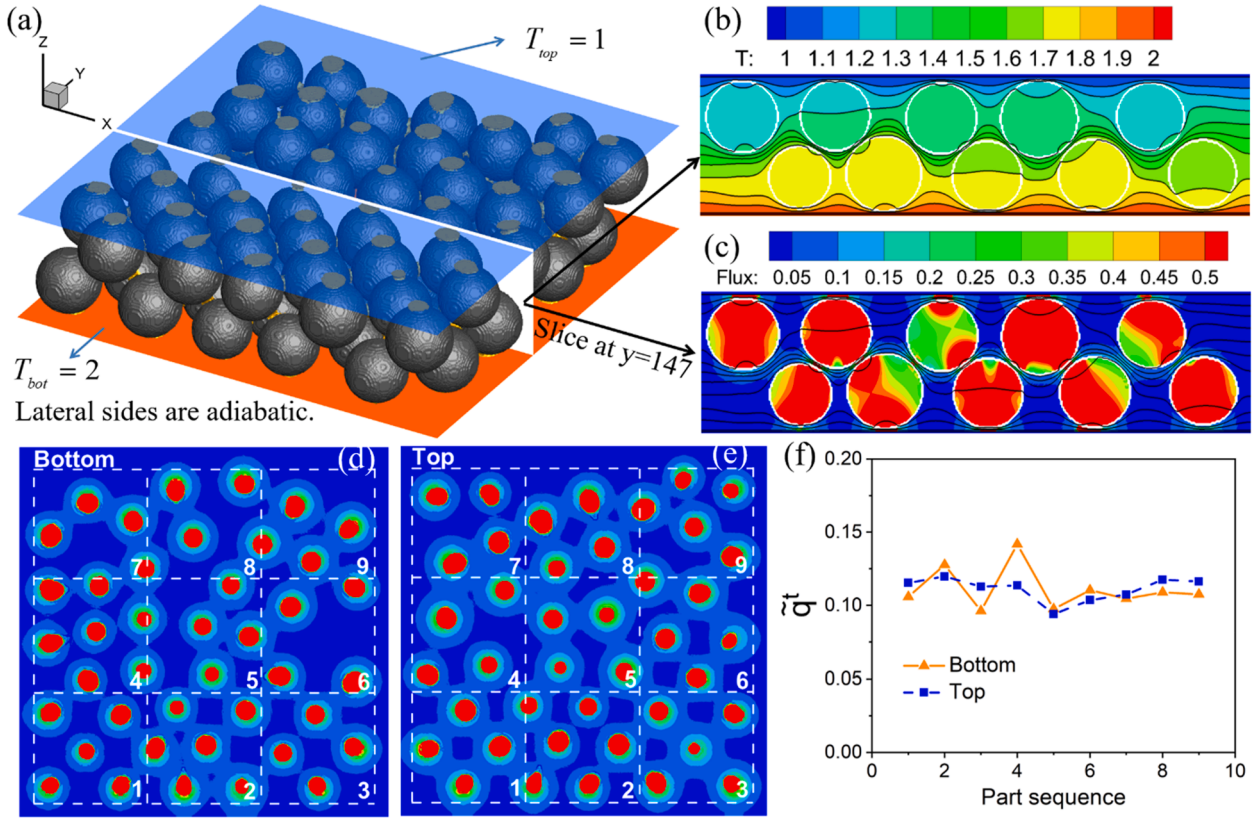

Fig. 3. Thermal performances of the neck-based thermal structure (NTS). (a) Simulation setup of NTS with the top and bottom temperatures $T_{top} = 1$ and $T_{bot} = 2$ and the four lateral sides adiabatic. (b) Temperature distribution with isolines (black) at the slice of y = 147 and the white lines denoting the boundaries of the filler particles. (c) Heat flux distribution at the slice of y = 147, with black lines being temperature isolines and white lines denoting the boundaries of filler particles. (d), (e) Heat flux at the bottom substrate and top cover with 9 equal-sized parts divided by white dash lines. (f) Normalized heat flux $\tilde{q}^t$ of 9 parts at bottom substrate and top cover.

2.3.2. Thermal performance of resultant NTS

After the validation of tricoupled hybrid LBM for neck formation by drying of colloidal suspension, we now validate the thermal LBM by evaluating the ETC of resultant NTS. The simulation setup is shown in Fig. 3a, where the top cover and bottom substrate temperatures are set as $T_{top} = 1$ and $T_{bot} = 2$, while the four lateral sides are set to be adiabatic to guarantee zero heat loss. In the experiment of [27], the filler particles are alumina with thermal conductivity of 30 W/mK, while the thermal conductivity of epoxy is 0.21 W/mK. The necks are compact, porous structures formed by deposited spherical alumina nanoparticles with two different diameters, i.e. 60% of the particles have a diameter of 40 nm and 40% a diameter of 250 nm. In [57], we used a thermal conductivity of the neck of 2.38 W/mK. Using these thermal conductivities, we can now simulate the heat transport. We note that the top cover and bottom substrate temperatures are reference temperature only for calculating ETC. Since ETC is determined under stationary state, its value is only dependent on the values of thermal conductivities of different materials, which are independent of the prescribed temperature.

To evaluate the heat conduction of the NTS, we choose slice y = 147 to analyze the temperature and heat flux. In Fig. 3b and c we can see the temperature and heat flux inside the filler particles. We observe that the temperature is more uniform and the heat flux in the filler particles is much larger than that in the epoxy, due to the high difference in their thermal conductivities. Fig. 3d and e show that, at both top cover and bottom substrate, high fluxes occur only at the locations of the necks, indicating the strong enhancement of heat conduction through the necks. To analyze the heat flux uniformity at the top and bottom chip layers, we divide each of them (excluding the periphery area) into 9 equal-sized parts and compare their normalized heat flux, i.e. $\tilde{q}^t(i) = q^t(i)/\sum_{i=1}^{9} q^t(i)$. Fig. 3f shows $\tilde{q}^t$ for the nine parts as indicated in Fig. 3d and e. We observe only a small fluctuation in $\tilde{q}^t$ due to the difference in filler particle and neck distribution, indicating that the heat flux distribution is generally quite uniform. The adiabatic boundary condition for four lateral sides does not induce an artificial inhomogeneous distribution of heat flux. Specifically, the standard deviations of $\tilde{q}^t$ of the 9 parts at top and bottom are only 0.008 and 0.014, with a mean value of 0.111. Finally, with the simulated temperature and heat flux, we calculate the ETC of the NTS to be 2.75 W/mK, which is close to the experimental result of 2.41 W/mK [27]. Similarly as in Section 2.3.1, to test the dependence on geometry, we have done simulations with three different FPCs with similar filler particle volume fraction $\tilde{V}^t_{fp} = 48.8\%, 48.0\%, 47.1\%$ in [57]. The corresponding ETCs are $\lambda_{eff} = 2.75, 2.78, 2.71$ W/mK, respectively. With an acceptable error of 14.1% in engineering, we conclude that we can apply this thermal LBM to study the heat conduction in NTSs formed under different conditions as shown in following Sections 3-5.

3. The influence of initial nanoparticle concentration

This first study looks at the influence of varying the initial colloidal particle concentration. The neck formation by drying of colloidal suspension in the cavity with micro-size filler particles is studied, and the thermal performance of the resulting NTSs is evaluated, with the initial nanoparticle concentration ϕ_{np}, assigned values of 1.6%, 2.3%, 3.0%, 3.7%. The simulation setup is the same as that in Section 2.3.1, to match the experimental conditions of [27].

3.1. Neck formation by colloidal nanoparticle deposition

For the cases of $\phi_{np} = 1.6\%, 2.3\%$ and 3.0%, the formed neck structures after drying of colloidal suspension are shown in Fig. 4a–c, while the result of $\phi_{np} = 3.7\%$ has already been given in Section 2. In the following we discusses necks formed at three different locations, i.e. $Neck_{p-t}$, $Neck_{p-b}$ and $Neck_{p-p}$ as defined in Section 2.3.1. To better analyze the overall nanoparticle deposition, we define the normalized total volume $\tilde{V}^t_{np}$ of all deposited nanoparticle as the ratio of total deposited nanoparticle volume V^t_{np} to the total volume of all filler particles V^t_{fp}, i.e. $\tilde{V}^t_{np} = V^t_{np}/V^t_{fp}$. The normalized total neck volume $\tilde{V}^t_{neck}$ is defined as the ratio of total volume of all necks V^t_{neck} and total filler particle volume V^t_{fp}, i.e. $\tilde{V}^t_{neck} = V^t_{neck}/V^t_{fp}$. The normalized volumes $\tilde{V}^t_{np}$ and $\tilde{V}^t_{neck}$ increase almost linearly with ϕ_{np} (see Fig. S2a in Supplementary Materials). The difference between $\tilde{V}^t_{np}$ and $\tilde{V}^t_{neck}$ indicates that a small portion of nanoparticles is also deposited on the surface of filler particles. Fig. 4d shows the neck amount versus nanoparticle

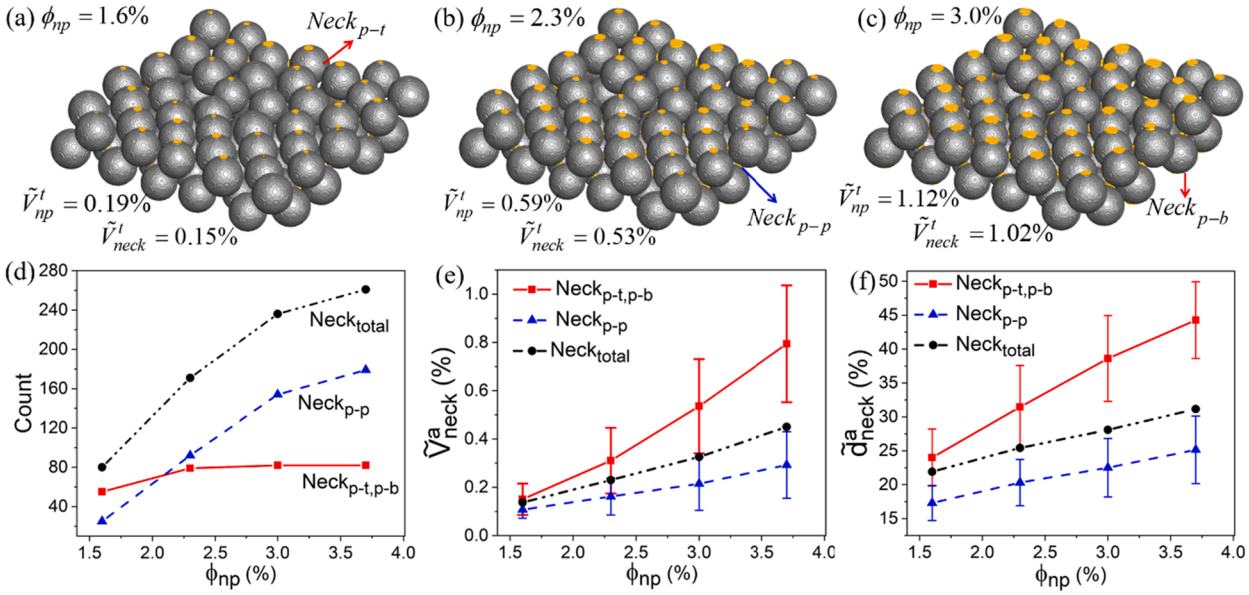

Fig. 4. Comparison of neck formation by drying of colloidal suspension with the initial nanoparticle concentration ranging from $\phi_{np} = 1.6\%, 2.3\%, 3.0\%$ to $\phi_{np} = 3.7\%$. (a)–(c) Neck formation with $\phi_{np} = 1.6\%, 2.3\%$ and 3.0%. (d) Comparison of total number of necks ($Neck_{total}$), necks at top/bottom ($Neck_{p-t,p-b}$) and necks between filler particles ($Neck_{p-p}$). (e)–(f) Comparison of normalized average neck volume ($\tilde{V}^a_{neck}$) and diameter ($\tilde{d}^a_{neck}$) including their variations.

concentration, where the neck count of $Neck_{p-t,p-b}$ reaches a maximum at $\phi_{np} = 2.3\%$, while the neck count of $Neck_{p-p}$ and $Neck_{total}$ increases at a decreasing rate not reaching maximum. The reason is that, for initial concentrations higher than $\phi_{np} = 2.3\%$, the potential positions for neck formations are almost filled up, and the remaining locations are the larger pores where it is more difficult to form necks. To further analyze the neck formation process, we define the normalized average neck volume $\widetilde{V}^a_{neck}$ as the ratio of average neck volume V^a_{neck} and average filler particle volume V^a_{fp}, i.e. $\widetilde{V}^a_{neck} = V^a_{neck}/V^a_{fp}$. Similarly, the normalized average neck diameter $\widetilde{d}^a_{neck}$ is defined as the ratio of average neck diameter d^a_{neck} and average filler particle diameter d^a_{fp}, i.e. $\widetilde{d}^a_{neck} = d^a_{neck}/d^a_{fp}$. Fig. 4e–f illustrates that, with nanoparticle concentration increasing from 1.6% to 3.7%, the normalized volumes $\widetilde{V}^a_{neck}$ for both $Neck_{p-t,p-b}$ and $Neck_{p-p}$ increase almost linearly from 0.15% and 0.11% to 0.79% and 0.29%, while the diameter $\widetilde{d}^a_{neck}$ for $Neck_{p-t,p-b}$ and $Neck_{p-p}$ increases almost linearly from 24.0% and 17.3% to 44.3% and 25.1%, respectively. In the experimental results obtained in a much larger cavity of 1 cm × 1 cm × 60 μm in [25], the diameter d^a_{neck} and number of necks $Neck_{p-b}$ are found to increase linearly with nanoparticle concentration, showing trends similar to the ones seen in our simulation results here.

In case of very low particle concentration such as $\phi_{np} = 0.8\%$ the simulations show that the nanoparticles basically attach to the surfaces of the filler particles and do not form necks. Current simulation results also show that, when the concentration is large, at $\phi_{np} = 4.6\%$ for instance, not only necks are formed but also the pore volumes between the filler particles are filled with nanoparticles, leading to a clogging of the pore structure. An illustration of the clogging of a pore in simulation with $\phi_{np} = 4.6\%$ is shown in Fig. 5a. Experimental results from [25] show similar clogging structures, as illustrated in Fig. 5b. This clogging may hinder the backfilling with epoxy in the final fabrication process, and thus a higher concentration over 4.6% may not be an optimal choice.

3.2. Thermal performance of resultant NTS

Further, the influence of the deposited necks on the heat conductivity of the resultant NTS is simulated and analyzed. The simulation setup is shown in Fig. 6a, which is the same as that in Section 2.3.2. Detailed comparisons of temperature and heat flux distributions are shown in Fig. 6b and c. With increasing nanoparticle concentration, the temperature distribution at the slice of y = 30 in Fig. 6b becomes more uniform at neck locations, indicating an improved heat conduction. In addition, the temperature in filler particles is much more uniform than that in the epoxy due to the large difference in thermal conductivity. In terms of the heat flux distribution in Fig. 6c, the heat flux increases obviously in the filler particles with increasing nanoparticle concentration, also indicating a better heat conduction. We also analyze the heat flux uniformity of the chip layers for different nanoparticle concentrations. As shown in Fig. S3 of Supplementary Materials, the normalized heat flux distributions are quite similar for different nanoparticle concentrations. A small deviation of the heat flux occurs at the lowest concentration $\phi_{np} = 1.6\%$ because no neck is formed at some locations due to a shortage of nanoparticles. The fluctuations of heat flux in different parts attribute to the heterogeneous distribution of filler particles and necks, as explained in Section 2.3.2.

With the simulated temperature and heat flux fields, we can evaluate the overall thermal performance of the NTS calculating the effective thermal conductivity (ETC). As shown in the right y-axis of Fig. 7, compared to the case of PTS (with no nanoparticles, $\phi_{np} = 0\%$) with ETC = 1.22 W/mK, the case of small concentration $\phi_{np} = 1.6\%$ with ETC = 1.81 W/mK shows an obvious improvement of 50%. By further increasing initial nanoparticle concentration from 1.6% to 3.7%, the ETC shows a further improvement but at a slightly decreased rate. The normalized total neck diameter $\widetilde{d}^t_{neck}$ in the left y-axis of Fig. 7 is defined as the product of total neck count $N(Neck_{total})$ and normalized average neck diameter $\widetilde{d}^a_{neck}$, i.e. $\widetilde{d}^t_{neck} = N(Neck_{total})*\widetilde{d}^a_{neck}$. Fig. 7 shows that the ETC agrees well with the normalized diameter $\widetilde{d}^t_{neck}$. The reason is that, the neck diameter, being an approximate to the square root of the contact area, reflects the heat conduction ability between adjacent filler particles, filler particle and top cover, filler particle and bottom substrate. This normalized total neck diameter can thus be considered a surrogate of contact area and a key indicator of ETC.

In summary, with the initial nanoparticle concentration increasing from 1.6% to 3.7%, the average neck volume and neck diameter increase almost linearly. The total number of necks also increases, but at a decreasing rate. As a result, the total neck diameter increases at a slightly reduced rate. The effective thermal conductivity of the resulted neck-based thermal structure follows the same trend of the total neck diameter. For initial concentrations lower than 0.8%, no complete neck is formed. Clogging structures occur at a concentration higher than 4.6%, which may not be optimal for heat conduction enhancement with respect to nanoparticle amount. Therefore, practically, we recommend an initial nanoparticle concentration over 0.8%. A high concentration of over 4.6% is still applicable but may not be optimal. The total neck diameter is proposed as an indicator of effective thermal conductivity.

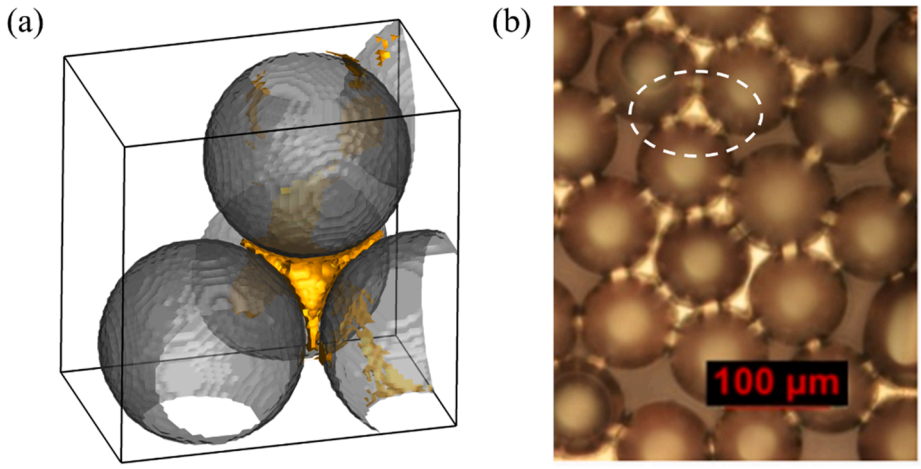

Fig. 5. Illustration of clogging of pore structure between filler particles by nanoparticle deposition. (a) Simulation result with a high initial concentration of $\phi_{np} = 4.6\%$. (b) Experimental observation from [25] (Reprint permission from *Journal of Microelectronics and Electronic Packaging*).

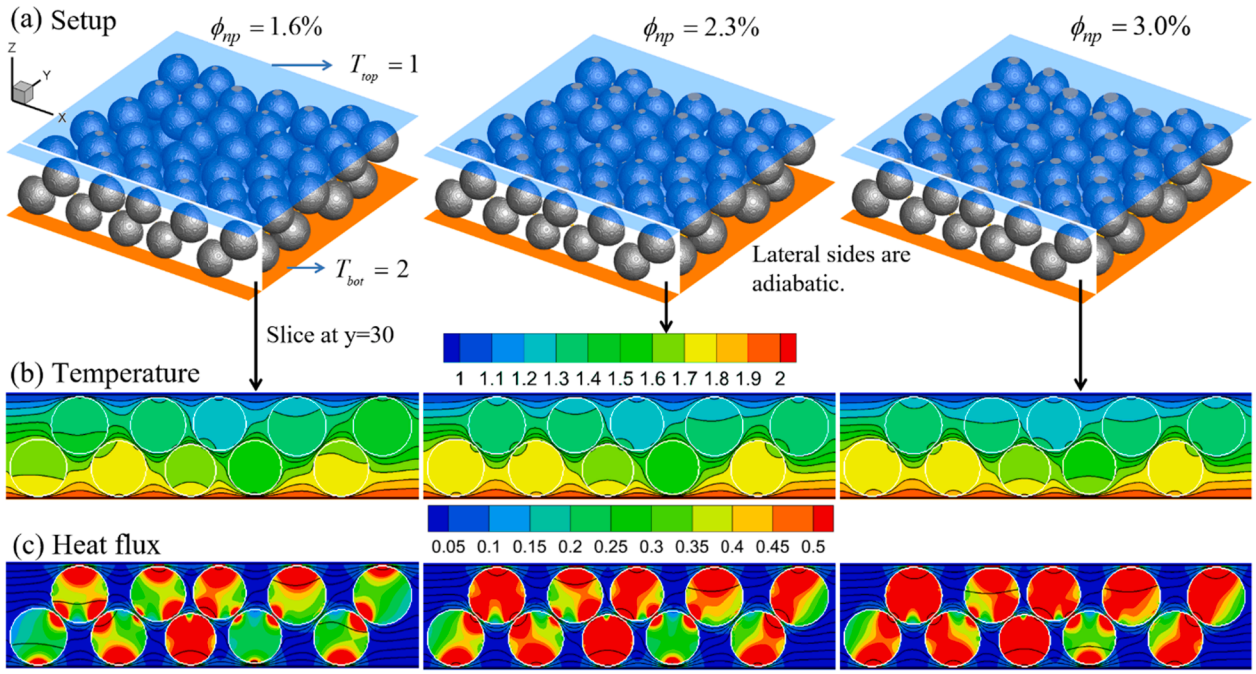

Fig. 6. Comparison of the thermal performance of the neck-based thermal structure (NTS) formed with different initial nanoparticle concentration ranging from $\phi_{np} = 1.6\%, 2.3\%$ to $\phi_{np} = 3.0\%$. (a) Simulation setup for heat conduction in NTS. (b) Comparison of temperature distribution with black temperature isolines at the slice of y = 30. (c) Comparison of heat flux distribution at the slice of y = 30 with the black lines indicating temperature isolines.

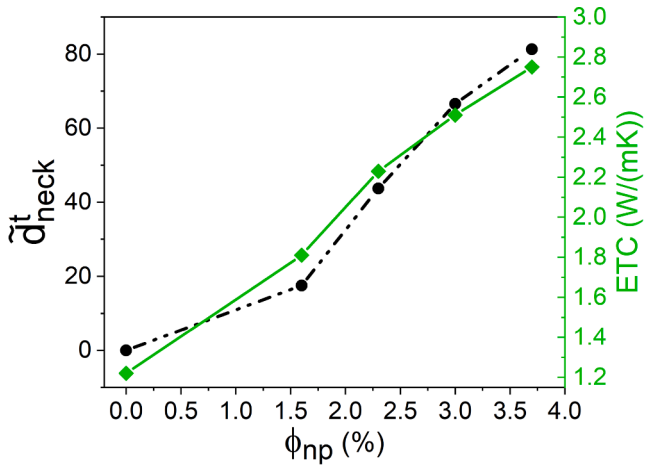

Fig. 7. Normalized total neck diameter ($\tilde{d}^t_{neck}$) and effective thermal conductivity (ETC) of neck-based thermal structure as functions of nanoparticle concentration (ϕ_{np}).

However, such diameter is quite difficult to be determined from experimental results showing a definite advantage of numerical simulations.

4. The influence of drying temperature

In this second study, the influence of drying temperature on the neck formation by drying of colloidal suspension in the cavity with micro-size filler particles is studied, and the thermal performance of resultant NTS is evaluated for a drying temperature varying from 25 °C(isothermal drying) to 43 °C, 60 °C, 80 °C and 100 °C. The initial concentration in all cases is 3.7%, and the surface wettability is uniform with a contact angle of 30°.

4.1. Neck formation by colloidal nanoparticle deposition

The necks formed at the temperature of 25 °C, 60 °C and 100 °C are shown in Fig. 8a. The necks become more uniform in size and distribution with increasing temperature. In contrast, as shown in Fig. 8b, the total number of necks, showing a mean value of 250 and a standard deviation of 3.6% (induced by the necks formed between filler particles), remains almost constant with increasing drying temperature. Fig. 8c shows the normalized average neck volume ($\tilde{V}^a_{neck}$) and standard variation (shaded area) for all necks ($Neck_{total}$), necks at top/bottom ($Neck_{p-t,p-b}$) and necks between filler particles ($Neck_{p-p}$). The normalized average neck volume $\tilde{V}^a_{neck}$ remains almost constant. The standard variation of normalized neck volume (shaded area) for $Neck_{p-t,p-b}$ and $Neck_{p-p}$, gradually decreases with increasing drying temperature. The decrease in standard deviation is higher in the temperature range 25 °C to 60 °C but slows down after 60 °C (especially after 80 °C), indicating the influence of drying temperature on neck formation at these temperatures becomes smaller. As seen in Fig. 8d, the normalized average neck diameter $\tilde{d}^a_{neck}$ shows the same trend as the normalized neck volume $\tilde{V}^a_{neck}$.

With increasing drying temperature, the temperature difference between the system and the environment also increases. The higher temperature difference leads to a higher pressure difference between the vapor at the liquid–vapor interface and the vapor in the environment, which increases the average drying rate. The average liquid drying rate Ep is defined as the total liquid mass m^t_l over the total drying time t^t_d (number of iterations in our simulation). Fig. S4a in Supplementary Materials shows that the total drying time decreases following a power function of the drying temperature T_d, indicating a linear increase of Ep (Fig. S4b in Supplementary Materials). In Fig. S4a, we can see the decrease in drying time is not as significant above 60 °C. Therefore, the drying temperature of 60 °C can be considered as the heating temperature to be used in practice for the drying of such kind of micro-porous structures since it is a good compromise between a short drying time and less energy consumption, while still ensuring a relatively uniform formation of necks.

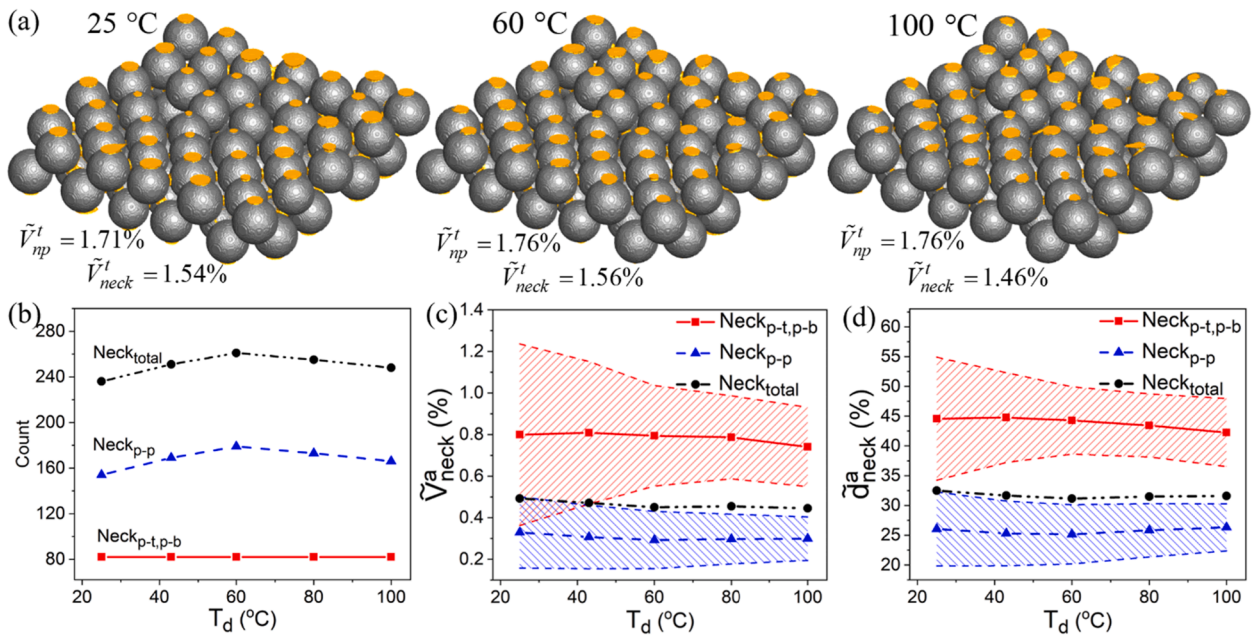

Fig. 8. Comparison of neck formation by drying of colloidal suspension in neck-based thermal structure as function of the drying temperature varying from 25 °C to 100 °C. (a) Neck formation at three drying temperatures. (b) Neck count of all necks ($Neck_{total}$), necks at top/bottom ($Neck_{p-t,p-b}$) and necks between filler particles ($Neck_{p-p}$). (c) Normalized average neck volume ($\tilde{V}^a_{neck}$) and variation (shaded area). (d) Normalized average neck diameter ($\tilde{d}^a_{neck}$) and variation (shaded area).

The minor influence of drying temperature on the total neck number and the dimensions of the necks, namely neck average or total diameter, average or total volume, stems from the following two facts. First, the total amount of nanoparticles for deposition is the same in all cases. Second, since the initial nanoparticle concentration (3.7%) is sufficiently high, necks can be formed easily between filler particles and thus the total neck number remains almost constant. The discussion above analyzes the overall neck distribution within the entire NTS. To analyze in more detail the neck size distribution over different locations, the NTS is divided into nine identical parts as shown in Fig. 9a. The influence of

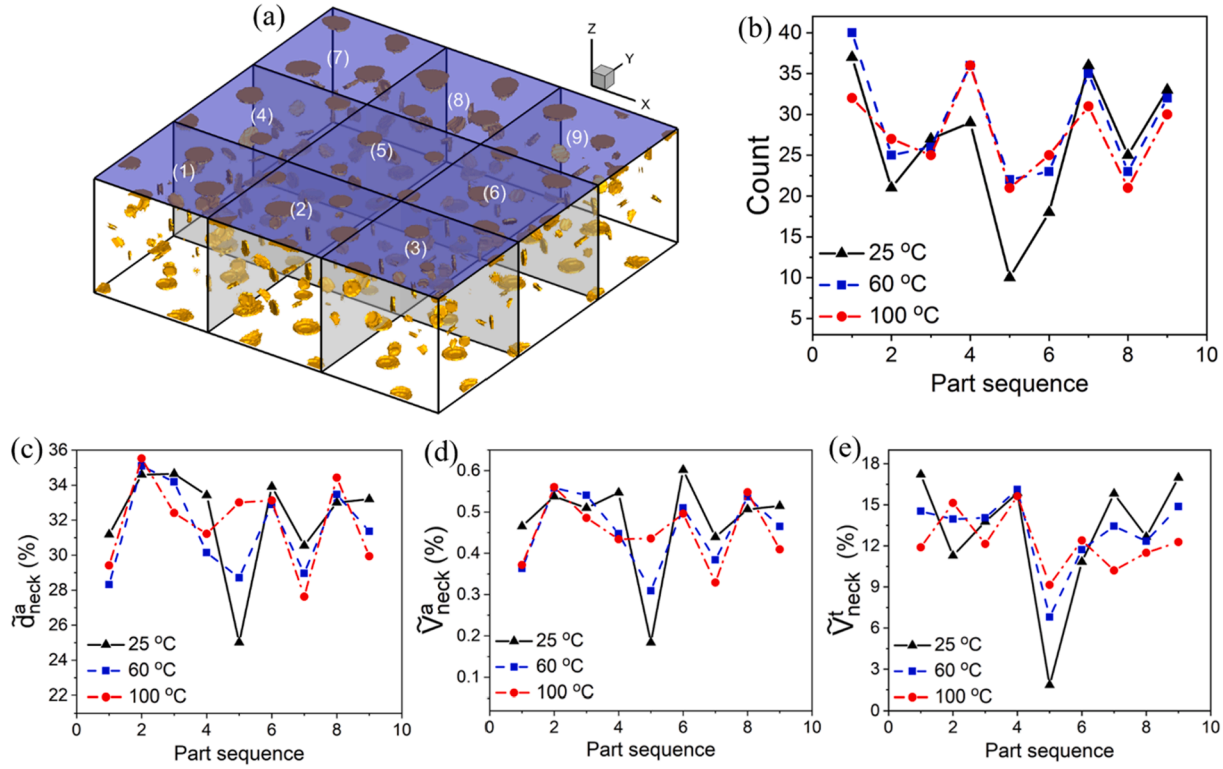

Fig. 9. Comparison of necks formed in different parts of the neck-based thermal structure (NTS) at drying temperature of 25 °C, 60 °C and 100 °C. (a) Illustration of the nine equally sized parts of NTS. (b) Distribution of number of necks $N(Neck)$ over nine parts. (c) Normalized average neck diameter $\tilde{d}^a_{neck}$. (d) Normalized average neck volume $\tilde{V}^a_{neck}$. (e) Normalized total neck volume $\tilde{V}^t_{neck}$.

drying temperature on neck formation is analyzed in these different parts. Fig. 9b–e show that at 25 °C, the number of necks, normalized average neck diameter $\widetilde{d}^{a}_{neck}$, average neck volume $\widetilde{V}^{a}_{neck}$ and total neck volume $\widetilde{V}^{t}_{neck}$ show quite high variations over the different parts, with a minimum in part five, i.e. in the center of the system. The explanation is as following. During this quasi-isothermal drying, the capillary forces are dominant, leading to the large pores being invaded first. Since the pores of large sizes are irregularly distributed over the sample, the drying pattern also becomes very irregular. As shown in Fig. 10a of the drying at 25 °C, the large pores in the center are firstly invaded (in red circle). Since the main evaporation fronts are at the lateral sides in parts 1–4 and 6–9, capillary flow occurs from the central large pores in part 5 to lateral sides (called capillary pumping) inducing a transport of nanoparticles from center to the lateral sides. Due to this transport, fewer nanoparticles are left in the central part and more nanoparticles are delivered to the peripheral parts, leading to the observed variation in neck size distribution. When the temperature increases, we note that the necks become more uniformly distributed between peripheral parts and the center one. This can be explained as follows. When the drying temperature increases, the liquid surface tension becomes smaller following an empirical equation of $\sigma = 0.2358(1 - T/T_c)^{1.256}[1 - 0.625(1 - T/T_c)]\ (N/m)$, where T_c is water critical temperature. As introduced in Section 2.3.1, the drying temperature T_d in simulations is obtained by applying the same relative temperature difference as in the experiment, i.e. $d\widetilde{T} = (T_d - T_{eq})/T_c \in (0, 0.115)$ for the 5 different drying temperatures ranging from 25 °C to 100 °C. The surface tension σ is plotted versus $\Delta\widetilde{T}$ in Fig. S5 in Supplementary Materials, for both simulation and the empirical equation. Both follow approximately a similar linear decrease and simulation results agree qualitatively well with the empirical equation. Quantitatively, the decrease of surface tension is not the same, because we are not able to simulate the real water–air density ratio of about 1000. In our simulations, the surface tension σ at (100 °C) is around 40% of that at isothermal condition (25 °C). Therefore, the capillary force $\Delta p = \sigma(1/r_1 + 1/r_2)cos\theta$ also decreases to 40%, where r_1, r_2.are the curvature radii of the pore and θ is the contact angle. As a result, the capillary pressure difference reduces by 40% and thus the capillary pumping effect becomes weaker [34]. On the other hand, the high temperature drives a high drying rate, making it more dominant than the capillary effect. In consequence, the drying pattern becomes continuous from the lateral sides to the center, as shown in Fig. 10b of drying at 100 °C. In addition, the drying time is reduced at higher temperature, which also leads to a smaller amount of nanoparticles transported. As a result, the distribution becomes more and more uniform with increasing drying temperature, as shown in Fig. 9b–e at 60 °C and 100 °C compared to 25 °C. We note that there are still fluctuations even at a drying temperature of 100 °C, since the pore size distribution is not equal in the different parts. To sum up, the transported nanoparticles at different drying temperature only change the size of necks at different locations, but the average neck size still remains globally constant in the system. Similar experimental results are obtained in [25] for a cavity of 1 cm × 1 cm × 60 μm with drying occurring only at two open ends. In this experiment, the system is divided into three identical parts, i.e. part one and three close to two open ends and part two in the middle. The observation is that, at a drying temperature of 25 °C, the necks are only formed in parts one and three, while at the drying temperature of 60 °C and 100 °C, the necks are formed nearly evenly in all three parts.

4.2. Thermal performance of resultant NTS

The influence of thermal necks formed at different drying temperatures on the heat conduction is shown in Fig. 11. Fig. 11a illustrates the simulation setup for modeling the heat conduction in NTS, as introduced in Section 2. The analyses of heat flux are given at two slices of y = 30 and y = 147 in Fig. 11b and c. These two slices are chosen with two reasons. First, at these two slices, the necks between the filler particles can be observed and their influences on heat conduction can be analyzed. Second, they are located one at the periphery and the other near the center of the system, allowing to compare the heat conduction heterogeneity in different parts of the system. To analyze the heat flux in different regions in this section, we normalize them by the total flux through the top cover, i.e. $\widetilde{q}^{t}_{area} = q^{t}_{area}/q^{t}_{top}$. In Fig. 11b and c we find that, when the drying temperature increases, the normalized heat flux through the filler particles in the white dashed area $\widetilde{q}^{t}_{w}$ (central part of the slice) decreases from 23.7% (lattice unit) to 19.6% and 17.7% at y = 30 while it increases from 14.7% to 17.8% and 20.7% at y = 147. The difference in heat flux at different locations is caused by the neck size difference as analyzed in the previous paragraph. For instance at 25 °C, the larger neck diameter at the slice of y = 30 leads to a higher normalized heat flux of 23.7% while the smaller neck diameter at the slice of y = 147 results in a lower heat flux of 14.7%. With this kind of compensation in heat flux at different locations induced by neck size difference, the overall heat conduction ability of NTS remains almost constant. As shown in the right y-axis of Fig. 12, at different drying temperatures, the ETC is almost constant showing that the influence of drying temperature on the thermal performance of NTS is very minor. The total normalized neck diameter $\widetilde{d}^{t}_{neck} = \widetilde{d}^{a}_{neck}(Neck_{total})*N(Neck_{total})$ in the left axis of Fig. 12 shows a good agreement with the ETC, showing that $d^{n,t}_{neck}$ is a good indicator to evaluate the overall thermal performance of resultant NTS, as explained in Section 3. The total normalized neck diameter $\widetilde{d}^{t}_{neck}$ remains also almost constant because both the normalized average neck diameter $\widetilde{d}^{a}_{neck}(Neck_{total})$ and the total neck count

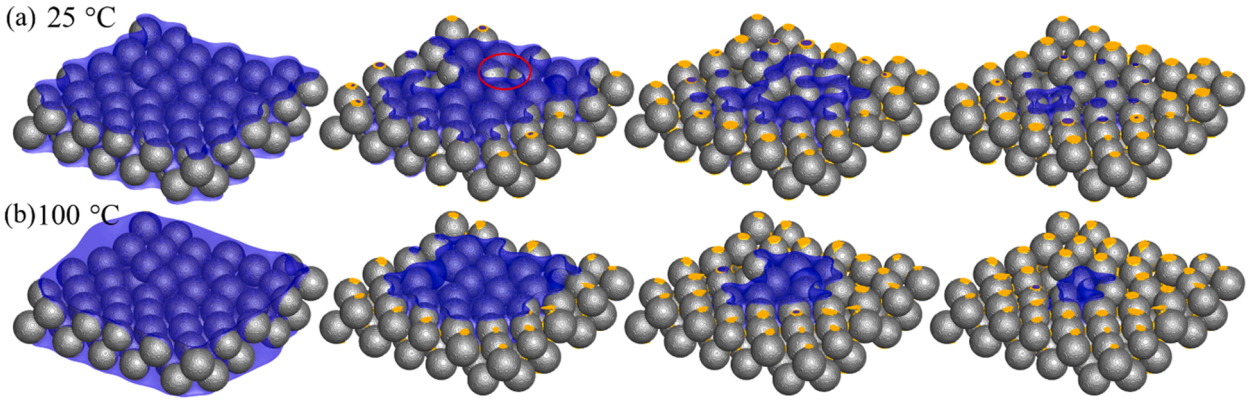

Fig. 10. Comparison of the drying processes of colloidal suspension at two different temperatures. (a) 25 °C (full drying process in Supplementary movie 2). (b) 100 °C (full drying process in Supplementary movie 3).

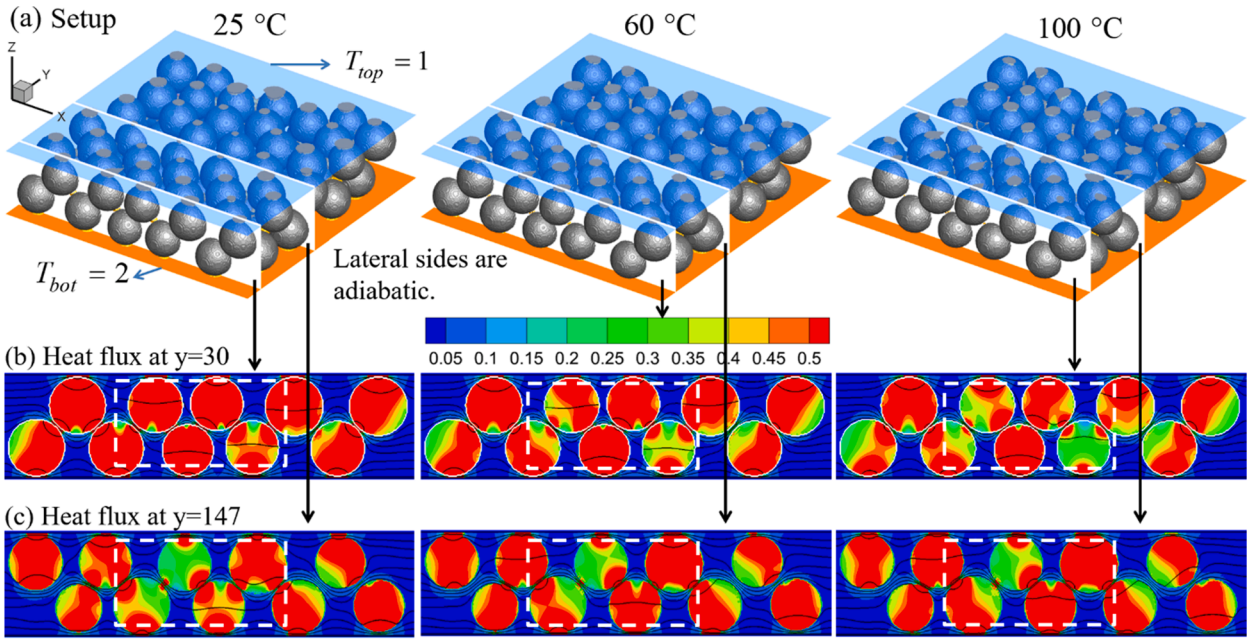

Fig. 11. Comparison of the thermal performance of neck-based thermal structure formed at the drying temperature of 25 °C, 60 °C and 100 °C. (a) Simulation setup for heat conduction. (b) and (c) Heat flux distribution at the slices of y = 30 and y = 147 with the black lines indicating temperature isolines. The size and heat flux are in lattice units.

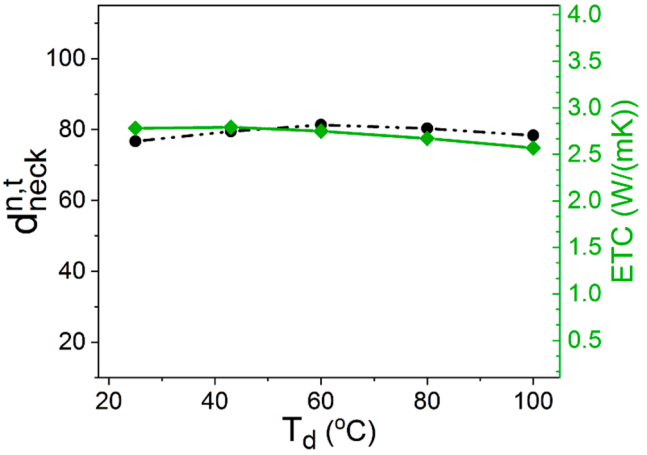

Fig. 12. Comparison of the normalized total neck diameter ($\widetilde{d}^{t}_{neck}$) and effective thermal conductivity (ETC) of neck-based thermal structure versus drying temperature (T_d).

$N(Neck_{total})$ vary very little, as shown in Fig. 8d and b. The comparison of total normalized neck volume $\widetilde{V}^{t}_{neck}$ and ETC is shown in Fig. S6 of Supplementary Materials, showing a worse agreement than that of $\widetilde{d}^{t}_{neck}$ and ETC.

Despite that the overall ETCs of the NTSs formed under different drying temperatures do not vary a lot, the heat conduction in different regions of the NTSs may be affected by the neck distribution, as described in Fig. 9. Fig. 13 shows that the normalized heat flux in the center (5th) part increases with drying temperature, leading to a more uniform heat flux distribution. This trend follows the analyses of neck sizes as shown above in Fig. 9, since necks play an important role in heat conduction. Although we have studied the influence of drying temperature on heat conduction of the resultant NTS only for the case of initial nanoparticle concentration $\phi_{np} = 3.7\%$, the results are representative of our studied concentration range (1.6%, 3.7%). This is because the normalized heat flux in each part of top and bottom surfaces only shows small changes for different concentrations, as shown in Fig. S3 in the Supplementary Materials. However, this may not be the case if the nanoparticle concentration is too large or too small, since clogging structures occur or necks are only formed at partial locations, resulting in different heat conductions.

In summary, with the drying temperature increasing from 25 °C to 100 °C, the average neck volume, diameter and number of necks remain almost constant. Consequently, the effective thermal conductivity shows a relatively constant trend. Nevertheless, the higher drying temperature leads to a more uniform neck size and distribution, as well as heat conduction. From the application field point of view, a drying temperature of 60 °C is recommended, since the formed necks are relatively uniform, the drying time is short and the energy consumption is not very high.

5. The influence of chip surface wettability

Finally, in this section, the influence of varying the substrate surface wettability is investigated. The neck formation by drying of a colloidal suspension is studied and the thermal performance of resultant NTS is evaluated by changing the wettability of chip surfaces, namely the top cover and bottom substrate of the cavity. The contact angle of both the top cover and the bottom substrate is changed from $CA_{t,b} = 15°$ to 120°, while the contact angle of filler particles remains unchanged at $CA_{fp} = 30°$, leading to a contact angle difference $CA_{t,b} - CA_{fp}$ ranging from −15° to 90°. In the drying simulations of this subsection, the initial nanoparticle concentration is $\phi_{np} = 3.7\%$ and the drying temperature is $T_d = 60$ °C.

5.1. Neck formation by colloidal nanoparticle deposition

Fig. 14a shows the simulation results of the necks formed by nanoparticle deposition at $CA_{t,b} - CA_{fp} = -15°$, 65° and 90°. As shown in the enlarged views in Fig. 14a, with increasing contact angle difference, more and more nanoparticles deposit at the middle height of the cavity between filler particles until clogging structures are formed. Meanwhile, less nanoparticles deposit at the top cover and bottom substrate until the necks disappear here. Fig. 14b shows the total number of necks

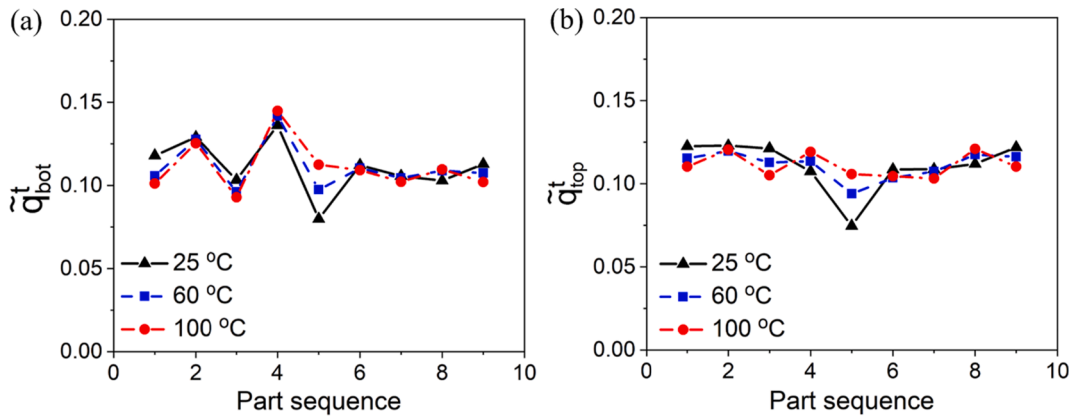

Fig. 13. Comparison of the normalized total heat flux ($\tilde{q}^t$) of 9 identical parts (Fig. 3d and e) at (a) bottom substrate and (b) top cover of the NTSs formed under different drying temperatures (25 °C, 60 °C and 100°C).

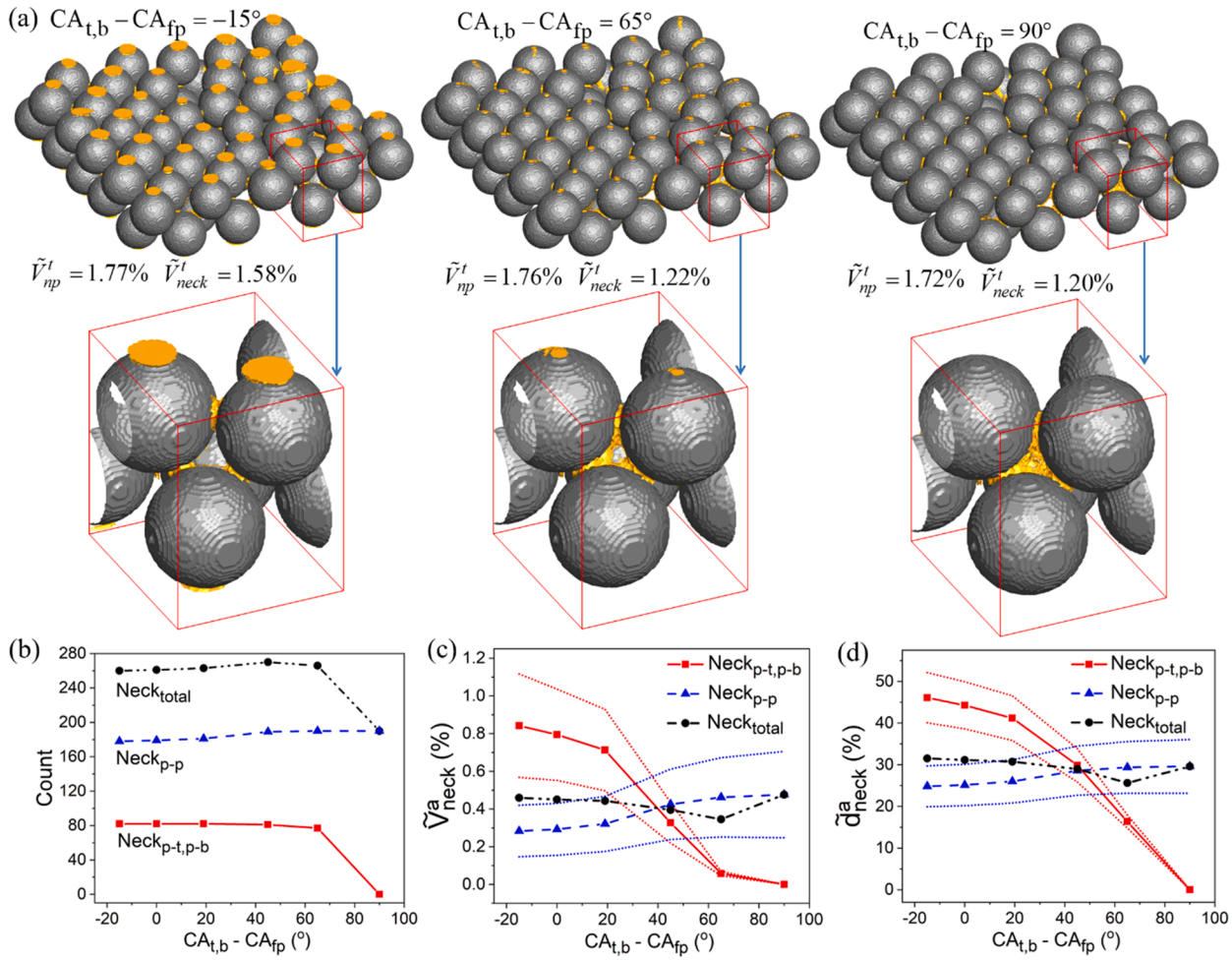

Fig. 14. Comparison of neck formation by drying of colloidal suspension with the contact angle difference of top cover/bottom substrate ($CA_{t,b}$) and filler particles (CA_{fp}) ranging from −15° to 90°. (a) Three cases of neck formation. (b) Comparison of total neck count ($Neck_{total}$), neck count at top/bottom ($Neck_{p-t,p-b}$) and between filler particles ($Neck_{p-p}$). (c) Comparison of normalized average neck volume $\tilde{V}^a_{neck}$ with its variation. (d) Comparison of normalized average neck diameter $\tilde{d}^a_{neck}$ with its variation.

($Neck_{total}$) barely changes below $CA_{t,b} - CA_{fp} = 65°$ and then decreases dramatically to the neck count between filler particles ($Neck_{p-p}$) at $CA_{t,b} - CA_{fp} = 90°$, where no neck is formed at top or bottom ($Neck_{p-t,p-b}$). The analyses of normalized average neck volume $\tilde{V}^a_{neck}$ and diameter $\tilde{d}^a_{neck}$ are shown in Fig. 14c and d. With increasing contact angle difference, the normalized average neck volume $\tilde{V}^a_{neck}$ of necks at top and bottom substrates ($Neck_{p-t,p-b}$) gradually decreases to zero, while $\tilde{V}^a_{neck}$ of necks in between the particles ($Neck_{p-p}$) increases only within a small range. The normalized average neck diameter $\tilde{d}^a_{neck}$ behaves similarly to

the corresponding normalized neck volume $\widetilde{V}^{a}_{neck}$.

We now explain the neck formation described above. With increasing contact angle difference, i.e. increase of the contact angle of top/bottom surfaces from 15° to 120°, the pressure at liquid–vapor meniscus at the top/bottom surfaces changes gradually. Assuming the vapor pressure in the environment is everywhere the same, the liquid pressure at the meniscus of top/bottom surfaces gradually increases due to the change in capillary pressure (induced by contact angle). The liquid pressure at the vapor–liquid menisci between the filler particles does not change, since the contact angle remains unchanged. Neglecting differences in pore size, the difference in capillary forces (capillary pumping pressure) for pores with different contact angles θ_a and θ_b is $\Delta p_a - \Delta p_b = \sigma(1/r_1 + 1/r_2)\,(cos\theta_a - cos\theta_b)$. Taking the contact angle difference of 90° as an example, e.g. chip surface contact angles of $\theta_a = 30°$ and $\theta_b = 120°$, we get a difference in capillary pressure of $\Delta p_a - \Delta p_b = 1.366\sigma(1/r_1 + 1/r_2)$. We normalize this difference by the capillary pressure for the condition of a uniform contact angle $\theta_a = 30°$, i.e. $\Delta p_a = 0.866\sigma(1/r_1 + 1/r_2)$, we get $(\Delta p_a - \Delta p_b)/\Delta p_a = 1.58$. Therefore, with increasing the contact angle difference of chip surfaces and filler particles to 90°, the capillary pumping pressure can be up to 1.58 times of the original capillary pressure with a uniform contact angle of 30°. Therefore, a flow between liquid at the meniscus of top/bottom surfaces and liquid at the menisci between filler particles is formed, transporting nanoparticles from the top/bottom to the middle height of the system. Fig. 15a shows the liquid configuration for the case with a contact angle difference of 90° at iteration of 24,000 during the drying process. In the half cross-section in Fig. 15b, the liquid–vapor menisci show that the surfaces at top/bottom are non-wetting with a contact angle of 120°, while the surface of filler particles is wetting with a contact angle of 30°, as imposed in the simulation. The red streamlines in Fig. 15c show the flow from the menisci at top/bottom plates to the menisci at middle height indicating the presence of capillary pumping. This mechanism explains the neck distribution discussed above in the previous paragraph. In addition to the important influence of contact angle difference on neck formation, we also analyze its influence on drying time, as well as drying rate. As shown in Fig. S7 of Supplementary Materials, only minor influence is seen on drying time and average drying rate at a high contact angle difference ($CA_{t,b}$ - $CA_{fp} \geqslant 65°$). The mechanism is the same as the neck formation explained above, i.e. capillary pumping is becoming stronger at higher contact angle difference, transporting liquid from the center of FPC (around top and bottom) to the periphery (middle height of FPC), which is beneficial for drying.

5.2. Thermal performance of resultant NTS

The influence of the contact angle difference on the heat conduction of the NTS is analyzed here. The simulation setup for modeling the heat conduction in NTS is shown in Fig. 16a. To analyze the heat transport, the temperature and heat flux distributions at a slice of y = 30 are compared for three contact angle differences, as shown in Fig. 16b and c. The temperature distribution is becoming less uniform in vertical direction for structures with higher contact angle difference and the heat flux decreases not only at the top/bottom, but also between filler particles. The reason is that, at higher contact angle difference, less or even no neck is formed at the top/bottom, leading to a decrease of the heat flux from bottom substrate to filler particles and from filler particles to top cover. Therefore, although the neck diameter in between the filler particles becomes larger, less heat is transported over the cavity. Except for the heat flux in vertical direction, we also analyze the heat flux at the top cover and bottom substrate, i.e. the chip layers. As shown in Fig. S8 of Supplementary Materials, the fluxes have some fluctuations in different parts, due to the heterogeneous distribution of filler particles and necks, as explained in Section 2.3.2. The normalized heat flux distributions are quite similar at a low contact angle difference ($CA_{t,b}$ - $CA_{fp} < 65°$). When the contact angle difference is getting higher, the neck size at top and bottom becomes very small (at

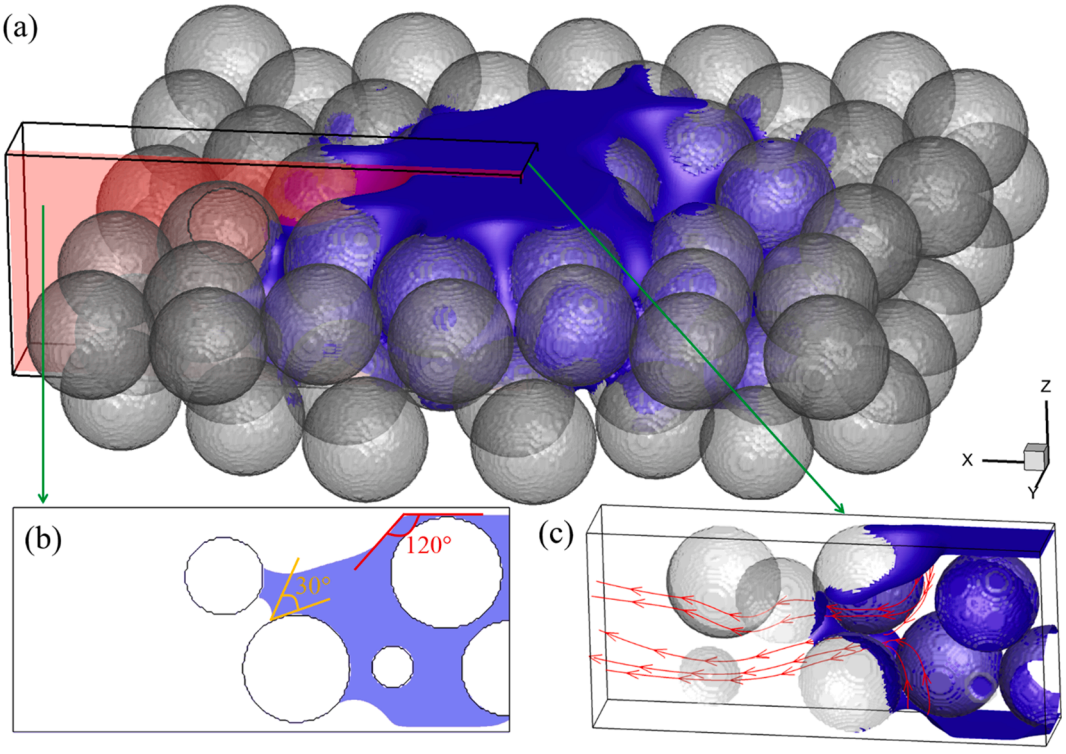

Fig. 15. Illustration of the capillary pumping in the system with contact angle difference of 90°. (a) Liquid configuration at the iteration of 24,000 (full drying process in Supplementary movie 4). (b) Menisci shapes at the slice of y = 230 showing hydrophobic surface (contact angle of 120°) at top/bottom plates and hydrophilic surfaces between filler particles (contact angle of 30°). (c) Capillary flow from the menisci at the top/bottom plates to the menisci between the filler particles at middle height.

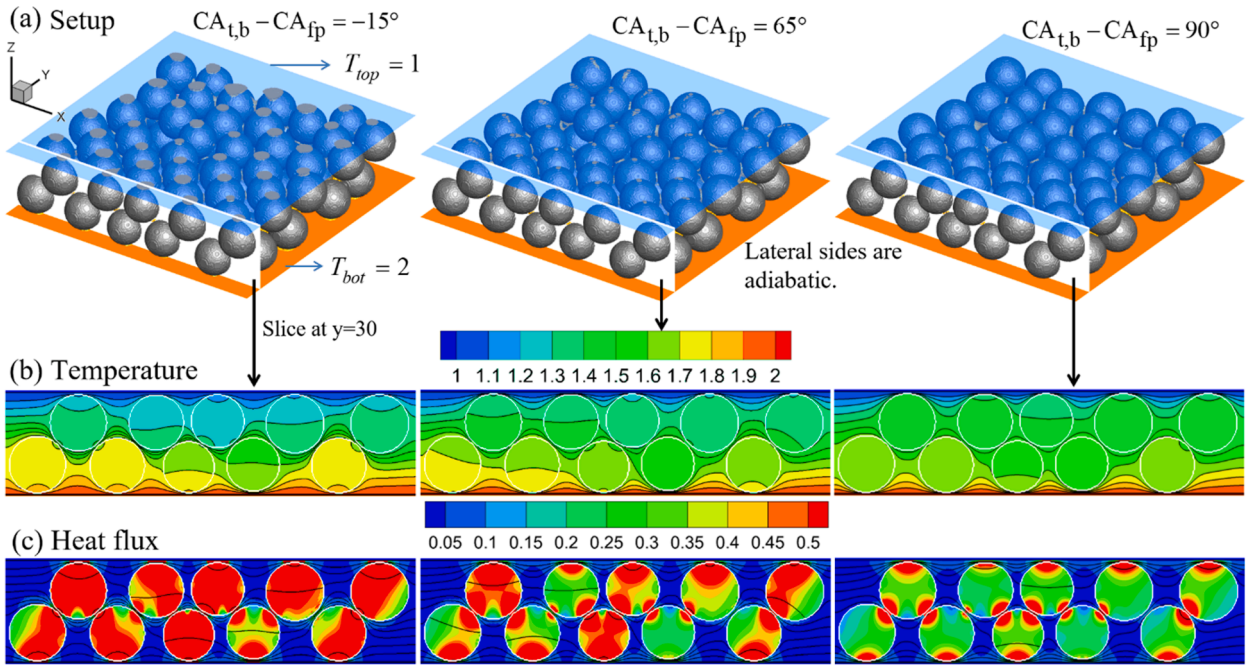

Fig. 16. Comparison of the thermal performance of the neck-base thermal structure with the contact angle difference of top cover/bottom substrate ($CA_{t,b}$) and filler particles (CA_{fp}) at −15°, 65° and 90°. (a) Simulation setup for heat conduction. (b) Comparison of temperature distribution with black temperature isolines at the slice of y = 30. (c) Comparison of flux distribution at the slice of y = 30 where the black lines indicating temperature isolines.

CA$_{t,b}$ - CA$_{fp}$ = 65°), or even disappears (at CA$_{t,b}$ - CA$_{fp}$ = 90°), as shown in Fig. 14a. Without necks, the material for heat conduction at top and bottom is purely epoxy, making the heat flux distribution more uniform.

In terms of the ETC representing the overall thermal performance of NTS, we can see that the ETC decreases at a higher rate with the increase of contact angle difference, as shown in the right y-axis of Fig. 17. Fig. 17 also shows that the ETC follows the trend of the normalized total neck diameter $\tilde{d}^t_{neck} = \tilde{d}^a_{neck}(Neck_{total})^*N(Neck_{total})$, as explained in Section 3. The decrease of $\tilde{d}^a_{neck}$ at a higher rate can be explained as follow. For contact angle difference varying from $CA_{t,b} - CA_{fp} = -15°$ to 65°, the decrease of normalized average neck diameter $\tilde{d}^a_{neck}(Neck_{total})$ is 19.4%, being more important than the increase of total neck count $N(Neck_{total})$ at 5.6%, as shown in Fig. 14b and d. The decrease of $\tilde{d}^a_{neck}(Neck_{total})$ with

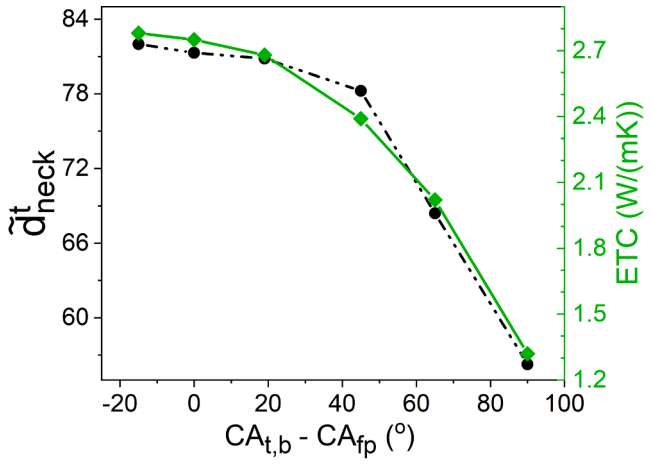

Fig. 17. Comparison of the normalized total neck diameter ($\tilde{d}^t_{neck}$) and effective thermal conductivity (ETC) of neck-based thermal structure versus contact angle difference ($CA_{t,b} - CA_{fp}$) of top cover/bottom substrate ($CA_{t,b}$) and filler particles (CA_{fp}).

an increased rate is due to the fact that nanoparticles are transported from the top/bottom to the middle height of the system by capillary pumping. As a result of this transport from top/bottom to middle height of the sample, the diameter of necks at top/bottom decreases from the periphery to the center of the neck, while the diameter of necks in the middle sample height increases at the neck periphery. Since the neck is concave being thick at the periphery and thin in center of the neck (illustrated in Fig. S9 in Supplementary Materials), the decrease of neck diameter at top/bottom is faster than the increase at middle height, as reflected in the slopes of $\tilde{d}^a_{neck}$ in Fig. 14d. The reason of the very small increase of the total number of necks $N(Neck_{total})$ is that most of the locations between filler particles or between filler particles and top/bottom are already formed with necks and it becomes more and more difficult to form new necks. At a contact angle difference of $CA_{t,b} - CA_{fp} = 90°$, the normalized average neck diameter $\tilde{d}^a_{neck}(Neck_{total})$ only increases slightly, while the number of necks $N(Neck_{total})$ decreases importantly. The slight increase in normalized average neck diameter $\tilde{d}^a_{neck}(Neck_{total})$ is because there are no necks at top/bottom, but only necks at middle height. The drop of total number of necks $N(Neck_{total})$ is also due to the fact that there is no neck at top/bottom. Similarly, the reason for having no neck at top/bottom is due to the strong capillary pumping at high contact angle difference, by which all the nanoparticles are transported from the top/bottom to the middle height of the system, as shown in Fig. 15c. We note that the ETC does not follow well the trend of the normalized total neck volume $\tilde{V}^t_{neck}$ since the neck shape is not regular (Fig. S9), as shown in Fig. S10 of Supplementary Materials.

In this section, we only consider the influences of varying the chip surface contact angle while keeping the filler particle contact angle unchanged. We mention that, if we keep the chip surface contact angle constant while increasing the filler particle contact angle, the neck formation will behave oppositely, i.e., neck size enlarges at chip surfaces while it fades between filler particles. Due to the decreased neck size between filler particles, the heat conduction decreases, as does the ETC of the resultant NTS. Figs. S11 and S12 in Supplementary Materials illustrate an example of the neck formation and heat conduction with the chip surface contact angle of 30° and the filler particle contact angle

of 75°.

In summary, the total average neck volume and diameter only slowly decrease with the contact angle difference between top/bottom and filler particles increasing from −15° to 65°, while the total number of necks remains almost constant. At a contact angle difference of 90°, no neck is formed anymore at the top and bottom substrates. Consequently, the total number of necks drops importantly, while the total average neck volume and diameter increase slightly. The change of neck size and number is due to the decrease of neck size at top/bottom and increase at the middle height of the system, due to the transport of nanoparticles by capillary pumping from the meniscus at top/bottom with high liquid pressure to the meniscus in the middle height with low liquid pressure. The total neck diameter decreases at a growing rate, due to the decrease of average neck diameter (before 65°) and the total number of necks (at 90°). Since the total neck diameter determines the overall heat conduction ability of the formed necks, the effective thermal conductivity shows a good agreement with the total neck diameter, i.e. decreasing at an increased rate. From the study of the influence of the contact angle difference, it is concluded that a uniform contact angle (30° here) of the entire system is optimal for the production of NTS considering a high thermal performance and low fabrication cost.

6. Conclusion

As an innovative technique, neck-based thermal structures (NTS) have shown the potential to enhance the heat conduction in 3D chip stacks by threefold experimentally. A critical step to produce the NTS lies in the neck formation by nanoparticle deposition after drying of colloidal suspension in the cavity filled with micro-size particles, since the thermal performance of the NTS is highly dependent on these neck structures. In this paper, the neck formation and the thermal performance of resultant NTS are numerically studied by a tricoupled hybrid LBM and a thermal LBM, focusing on the influence of initial nanoparticle concentration, drying temperature and chip surface wettability.

First, the influence of initial particle concentration is studied. With increasing nanoparticle concentration from 1.6% to 3.7%, the average neck volume and diameter increase almost linearly. The total number of necks increases also, but at a decreasing rate. The effective thermal conductivity (ETC) of the resulting neck-based thermal structure increases at a slightly reduced rate. No neck is formed at an initial concentration lower than 0.8%, while clogging structures occur at an initial concentration of 4.6%. Second, the influence of drying temperature is discussed. With increasing drying temperature from $25°C$ to $100°C$, the average neck volume, diameter and number of necks remain almost constant. Consequently, the ETC of the resulted NTS shows also a relatively constant trend. Nevertheless, a higher drying temperature leads to a more uniform neck size and distribution. Practically, a drying temperature of $60°C$ is suggested, since it results in the necks being relatively uniformly distributed, the drying time being short and the energy consumption being not too high. Finally, the influence of chip surface wettability is investigated. With the contact angle difference of chip surface (top/bottom of the cavity) and filler particles (remaining at 30°) increasing from −15° to 65°, the average neck volume and diameter decrease slowly while the total number of necks remains almost constant. At a contact angle difference of 90°, no neck is formed at the top and bottom and the total number of necks drops dramatically while the average neck volume and diameter increase slightly. With the contact angle difference increasing from −15° to 90°, the ETC decreases at a growing rate, due to the decrease of average neck diameter up to 65° and decrease of total number of necks at 90°. A higher wettability of the chip surface leads to slightly larger neck diameters at the top/bottom of the cavity, resulting in an overall small increase in heat conduction. A uniform contact angle of the entire system at 30° is suggested for the production of NTS showing optimal thermal performance and low fabrication cost.

In summary, the parametric study of initial nanoparticle concentration, drying temperature and chip surface wettability shows that the numerical models of tricoupled hybrid LBM and thermal LBM can reveal the multiple mechanisms at play and can offer great assistance in the design of these structures in real complex engineering applications.

Author contributions

F. Q., D. D. and J. C conceived the project. F. Q. performed the simulations and wrote the paper. All the authors analyzed the data and discussed the results. All authors have made comments and given approval to the final version of the manuscript.

Funding sources

Swiss National Science Foundation (SNF, project No. 160189 and No. 175793).

Declaration of Competing Interest

The authors declare that they have no known competing financial interests or personal relationships that could have appeared to influence the work reported in this paper.

Acknowledgement

LANL's Institutional Computing Program and the Swiss National Super Computing Center (Project No. s823) are acknowledged for providing the computing support. Dr. Omid Dorostkar is acknowledged for the assistance of the assembly of filler particles. Mr. Robert Fischer is acknowledged for helping to analyze the neck structures.

Appendix A. Supplementary material

Supplementary data to this article can be found online at https://doi.org/10.1016/j.applthermaleng.2021.116585.

References

[1] R. Michael Lea, A 3-d stacked chip packaging solution for miniaturized massively parallel processing, IEEE Trans. Adv. Packag. 22 (1999) 424–432, https://doi.org/10.1109/6040.784496.

[2] J.U. Knickerbocker, P.S. Andry, B. Dang, R.R. Horton, M.J. Interrante, C.S. Patel, R. J. Polastre, K. Sakuma, R. Sirdeshmukh, E.J. Sprogis, S.M. Sri-Jayantha, A. M. Stephens, A.W. Topol, C.K. Tsang, B.C. Webb, S.L. Wright, Three-dimensional silicon integration, IBM J. Res. Dev. 52 (2008) 553–569, https://doi.org/10.1147/JRD.2008.5388564.

[3] L.C. Shen, C.W. Chien, H.C. Cheng, C. Te Lin, Development of three-dimensional chip stacking technology using a clamped through-silicon via interconnection, Microelectron. Reliab. 50 (2010) 489–497, https://doi.org/10.1016/j.microrel.2009.10.012.

[4] V. Venkatadri, B. Sammakia, K. Srihari, D. Santos, A review of recent advances in thermal management in three dimensional chip stacks in electronic systems, J. Electron. Packag. Trans. ASME. 133 (2011), https://doi.org/10.1115/1.4005298.

[5] T. Ohba, Y. Kim, Y. Mizushima, N. Maeda, K. Fujimoto, S. Kodama, Review of wafer-level three-dimensional integration (3DI) using bumpless interconnects for tera-scale generation, IEICE Electron. Express. 12 (2015) 1–14, https://doi.org/10.1587/elex.12.20152002.

[6] I.A.M. Elfadel, 3D Stacked Chips, 2016. https://doi.org/10.1007/978-3-319-20481-9.

[7] W.W. Shen, K.N. Chen, Three-dimensional integrated circuit (3D IC) key technology: through-silicon via (TSV), Nanoscale Res. Lett. 12 (2017), https://doi.org/10.1186/s11671-017-1831-4.

[8] I.A.M. Elfadel, G. Fettweis, 3D Stacked Chips: From Emerging Processes to Heterogeneous Systems, Springer International Publishing, 2016 https://doi.org/10.1007/978-3-319-20481-9.

[9] A. Srivastava, Academic press library in signal processing, in: Elsevier Masson SAS, 2014, pp. 629–632. https://doi.org/10.1016/b978-0-12-396501-1.00022-4.

[10] S.G. Kandlikar, W.J. Grande, Evaluation of single phase flow in microchannels for high heat flux chip cooling-thermohydraulic performance enhancement and fabrication technology, Heat Transf. Eng. 25 (2004) 5–16, https://doi.org/10.1080/01457630490519772.

[11] A. Habibi Khalaj, S.K. Halgamuge, A Review on efficient thermal management of air- and liquid-cooled data centers: from chip to the cooling system, Appl. Energy. 205 (2017) 1165–1188, https://doi.org/10.1016/j.apenergy.2017.08.037.

[12] S. Wiriyasart, C. Hommalee, P. Naphon, Thermal cooling enhancement of dual processors computer with thermoelectric air cooler module, Case Stud. Therm. Eng. 14 (2019) 100445, https://doi.org/10.1016/j.csite.2019.100445.

[13] D.B. Tuckerman, R.F.W. Pease, High-performance heat sinking for VLSI, IEEE Electron Device Lett. EDL-2 (1981) 126–129, https://doi.org/10.1109/EDL.1981.25367.

[14] H. Oprins, G. Van der Veken, C.C.S. Nicole, C.J.M. Lasance, M. Baelmans, On-chip liquid cooling with integrated pump technology, IEEE Trans. Components Packag. Technol. 30 (2007) 209–217, https://doi.org/10.1109/TCAPT.2007.898301.

[15] B. Dang, M.S. Bakir, D.C. Sekar, C.R. King, J.D. Meindl, Integrated microfluidic cooling and interconnects for 2D and 3D chips, IEEE Trans. Adv. Packag. 33 (2010) 79–87, https://doi.org/10.1109/TADVP.2009.2035999.

[16] T. Gao, S. Shao, Y. Cui, B. Espiritu, C. Ingalz, H. Tang, A. Heydari, A study of direct liquid cooling for high-density chips and accelerators, in: Proc. 16th Intersoc. Conf. Therm. Thermomechanical Phenom. Electron. Syst. ITherm 2017, 2017, pp. 565–573. https://doi.org/10.1109/ITHERM.2017.7992537.

[17] A.A.Y. Al-Waaly, M.C. Paul, P. Dobson, Liquid cooling of non-uniform heat flux of a chip circuit by subchannels, Appl. Therm. Eng. 115 (2017) 558–574, https://doi.org/10.1016/j.applthermaleng.2016.12.061.

[18] Y. Joshi, Zhimin Wan, Handbook of Thermal Science and Engineering, Springer International Publishing, 2017 https://doi.org/10.1007/978-3-319-32003-8.

[19] W. Qu, I. Mudawar, Transport phenomena in two-phase micro-channel heat sinks, J. Electron. Packag. Trans. ASME. 126 (2004) 213–224, https://doi.org/10.1115/1.1756145.

[20] A. Radwan, S. Ookawara, S. Mori, M. Ahmed, Uniform cooling for concentrator photovoltaic cells and electronic chips by forced convective boiling in 3D-printed monolithic double-layer microchannel heat sink, Energy Convers. Manag. 166 (2018) 356–371, https://doi.org/10.1016/j.enconman.2018.04.037.

[21] T.G. Karayiannis, M.M. Mahmoud, Flow boiling in microchannels: fundamentals and applications, Appl. Therm. Eng. 115 (2017) 1372–1397, https://doi.org/10.1016/j.applthermaleng.2016.08.063.

[22] C. Falsetti, M. Magnini, J.R. Thome, Hydrodynamic and thermal analysis of a micro-pin fin evaporator for on-chip two-phase cooling of high density power micro-electronics, Appl. Therm. Eng. 130 (2018) 1425–1439, https://doi.org/10.1016/j.applthermaleng.2017.10.117.

[23] M.S. Bakir, J.D. Meindl, Integrated Interconnect Technologies for 3D Nanoelectronic Systems, 2008.

[24] R. Muwanga, I. Hassan, R. MacDonald, Characteristics of flow boiling oscillations in silicon microchannel heat sinks, J. Heat Transfer. 129 (2007) 1341–1351, https://doi.org/10.1115/1.2754946.

[25] T. Brunschwiler, G. Schlottig, S. Ni, Y. Liu, J.V. Goicochea, J. Zürcher, H. Wolf, Formulation of percolating thermal underfills using hierarchical self-assembly of microparticles and nanoparticles by centrifugal forces and capillary bridging, J. Microelectron. Electron. Packag. 9 (2012) 149–159, https://doi.org/10.4071/imaps.357.

[26] G. Hong, T.M. Schutzius, S. Zimmermann, B.R. Burg, J. Zürcher, T. Brunschwiler, G. Tagliabue, B. Michel, D. Poulikakos, In situ assembly in confined spaces of coated particle scaffolds as thermal underfills with extraordinary thermal conductivity, ACS Appl. Mater. Interfaces. 7 (2015) 838–844, https://doi.org/10.1021/am5073222.

[27] T. Brunschwiler, J. Zürcher, L. Del Carro, G. Schlottig, B. Burg, S. Zimmermann, U. Zschenderlein, B. Wunderle, F. Schindler-Saefkow, R. Stässle, Review on percolating and neck-based underfills for three-dimensional chip stacks, J. Electron. Packag. 138 (2016) 41009, https://doi.org/10.1115/1.4034927.

[28] J. Zurcher, X. Chen, B.R. Burg, S. Zimmermann, R. Straessle, A.R. Studart, T. Brunschwiler, Enhanced percolating thermal underfills achieved by means of nanoparticle bridging necks, IEEE Trans. Components, Packag. Manuf. Technol. 6 (2016) 1785–1795, https://doi.org/10.1109/TCPMT.2016.2614537.

[29] R. Straessle, S. Zimmermann, L. Carro, S. Member, J. Zürcher, S. Member, G. Schlottig, A. Achen, G. Hong, D. Poulikakos, T. Brunschwiler, S. Member, Percolating microparticles applied as underfill, IEEE Trans. Components Packag. Technol. 8 (2018) 840–850.

[30] F. Qin, A. Mazloomi Moqaddam, Q. Kang, D. Derome, J. Carmeliet, Entropic multiple-relaxation-time multirange pseudopotential lattice Boltzmann model for two-phase flow, Phys. Fluids. 30 (2018), https://doi.org/10.1063/1.5016965.

[31] A.M. Mazloomi, S.S. Chikatamarla, I.V. Karlin, Entropic lattice Boltzmann method for multiphase flows, Phys. Rev. Lett. 114 (2015) 174502, https://doi.org/10.1103/PhysRevLett.114.174502.

[32] S. Son, L. Chen, D. Derome, J. Carmeliet, Numerical study of gravity-driven droplet displacement on a surface using the pseudopotential multiphase lattice Boltzmann model with high density ratio, Comput. Fluids. 117 (2015) 42–53, https://doi.org/10.1016/j.compfluid.2015.04.022.

[33] A. Montessori, P. Prestininzi, M. La Rocca, S. Succi, Entropic lattice pseudo-potentials for multiphase flow simulations at high Weber and Reynolds numbers, Phys. Fluids. 29 (2017), https://doi.org/10.1063/1.5001253.

[34] F. Qin, L. Del Carro, A. Mazloomi Moqaddam, Q. Kang, T. Brunschwiler, D. Derome, J. Carmeliet, Study of non-isothermal liquid evaporation in synthetic micro-pore structures with hybrid lattice Boltzmann model, J. Fluid Mech. 866 (2019) 33–60, https://doi.org/10.1017/jfm.2019.69.

[35] I.V. Karlin, D. Sichau, S.S. Chikatamarla, Consistent two-population lattice Boltzmann model for thermal flows, Phys. Rev. E - Stat. Nonlinear, Soft Matter Phys. 88 (2013) 1–13, https://doi.org/10.1103/PhysRevE.88.063310.

[36] X. Shan, Simulation of Rayleigh-B\'enard convection using lattice Boltzmann method, Phys. Rev. E. 55 (1997) 20, https://doi.org/10.1103/PhysRevE.55.2780.

[37] Q. Li, K.H. Luo, Q.J. Kang, Y.L. He, Q. Chen, Q. Liu, Lattice Boltzmann methods for multiphase flow and phase-change heat transfer, Prog. Energy Combust. Sci. 52 (2016) 62–105, https://doi.org/10.1016/j.pecs.2015.10.001.

[38] A.J.C. Ladd, R. Verberg, Lattice-Boltzmann simulations of particle-fluid suspensions, J. Stat. Phys. 104 (2001) 1191–1251, https://doi.org/10.1023/A:1010414013942.

[39] F. Qin, A. Mazloomi Moqaddam, L. Del Carro, Q. Kang, T. Brunschwiler, D. Derome, J. Carmeliet, Tricoupled hybrid lattice Boltzmann model for nonisothermal drying of colloidal suspensions in micropore structures, Phys. Rev. E. 99 (2019), https://doi.org/10.1103/PhysRevE.99.053306.

[40] F. Qin, A. Mazloomi Moqaddam, Q. Kang, D. Derome, J. Carmeliet, LBM simulation of self-assembly of clogging structures by evaporation of colloidal suspension in 2D porous media, Transp. Porous Media. (2018) 1–15, https://doi.org/10.1007/s11242-018-1157-4.

[41] M. Zhao, X. Yong, Nanoparticle motion on the surface of drying droplets, Phys. Rev. Fluids. 3 (2018) 1–16, https://doi.org/10.1103/PhysRevFluids.3.034201.

[42] Q. Kang, L. Chen, A.J. Valocchi, H.S. Viswanathan, Pore-scale study of dissolution-induced changes in permeability and porosity of porous media, J. Hydrol. 517 (2014) 1049–1055, https://doi.org/10.1016/j.jhydrol.2014.06.045.

[43] J. Zhao, Q. Kang, J. Yao, H. Viswanathan, R. Pawar, L. Zhang, H. Sun, The effect of wettability heterogeneity on relative permeability of two-phase flow in porous media: a lattice Boltzmann study, Water Resour. Res. 54 (2018) 1295–1311, https://doi.org/10.1002/2017WR021443.

[44] H. Liu, Q. Kang, C.R. Leonardi, S. Schmieschek, A. Narváez, B.D. Jones, J. R. Williams, A.J. Valocchi, J. Harting, Multiphase lattice Boltzmann simulations for porous media applications – a review, Comput. Geosci. (2016) 777–805, https://doi.org/10.1007/s10596-015-9542-3.

[45] M. Wang, J. Wang, N. Pan, S. Chen, Mesoscopic predictions of the effective thermal conductivity for microscale random porous media, Phys. Rev. E - Stat. Nonlinear, Soft Matter Phys. 75 (2007) 1–10, https://doi.org/10.1103/PhysRevE.75.036702.

[46] M. Wang, Q. Kang, N. Pan, Thermal conductivity enhancement of carbon fiber composites, Appl. Therm. Eng. 29 (2009) 418–421, https://doi.org/10.1016/j.applthermaleng.2008.03.004.

[47] X. Chen, P. Han, A note on the solution of conjugate heat transfer problems using SIMPLE-like algorithms, Int. J. Heat Fluid Flow. 21 (2000) 463–467, https://doi.org/10.1016/S0142-727X(00)00028-X.

[48] M. Prat, Recent advances in pore-scale models for drying of porous media, Chem. Eng. J. 86 (2002) 153–164, https://doi.org/10.1016/S1385-8947(01)00283-2.

[49] I.U. Vakarelski, D.Y.C. Chan, T. Nonoguchi, H. Shinto, K. Higashitani, Assembly of gold nanoparticles into microwire networks induced by drying liquid bridges, Phys. Rev. Lett. 102 (2009) 100–103, https://doi.org/10.1103/PhysRevLett.102.058303.

[50] J. Perelaer, P.J. Smith, C.E. Hendriks, A.M.J. Van Den Berg, U.S. Schubert, The preferential deposition of silica micro-particles at the boundary of inkjet printed droplets, Soft Matter. 4 (2008) 1072–1078, https://doi.org/10.1039/b715076h.

[51] S.A. Ryu, J.Y. Kim, S.Y. Kim, B.M. Weon, Drying-mediated patterns in colloid-polymer suspensions, Sci. Rep. 7 (2017) 1–7, https://doi.org/10.1038/s41598-017-00932-z.

[52] M. Su, Z. Huang, Y. Li, X. Qian, Z. Li, X. Hu, Q. Pan, F. Li, L. Li, Y. Song, A 3D self-shaping strategy for nanoresolution multicomponent architectures, Adv. Mater. 30 (2018) 1–8, https://doi.org/10.1002/adma.201703963.

[53] H.P. Huinink, L. Pel, M.A.J. Michels, M. Prat, Drying processes in the presence of temperature gradients - Pore-scale modelling, Eur. Phys. J. E. 9 (2002) 487–498, https://doi.org/10.1140/epje/i2002-10106-1.

[54] N. Vorhauer, T. Metzger, E. Tsotsas, M. Prat, Temperature gradient induced double stabilization of the evaporation front within a drying porous medium, Phys. Rev. Fluids. 2018 (2012) 1–24, https://doi.org/10.1103/PhysRevFluids.3.114201.

[55] D. Or, P. Lehmann, E. Shahraeeni, N. Shokri, Advances in soil evaporation physics—a review, Vadose Zo. J. 12 (2013), https://doi.org/10.2136/vzj2012.0163.

[56] P. Coussot, Scaling approach of the convective drying of a porous medium, Eur. Phys. J. B. 15 (2000) 557–566, https://doi.org/10.1007/s100510051160.

[57] F. Qin, J. Zhao, Q. Kang, T. Brunschwiler, D. Derome, Lattice Boltzmann modeling of heat conduction enhancement by colloidal nanoparticle deposition in micro-porous structures, Submitt. to Phys. Rev. E. (2020) 1–46.

[58] F. Qin, M. Su, J. Zhao, A. Mazloomi Moqaddam, L. Del Carro, T. Brunschwiler, Q. Kang, Y. Song, D. Derome, J. Carmeliet, Controlled 3D nanoparticle deposition by drying of colloidal suspension in designed thin micro-porous architectures, Int. J. Heat Mass Transf. 158 (2020) 120000, https://doi.org/10.1016/j.ijheatmasstransfer.2020.120000.

[59] M. Sbragaglia, R. Benzi, L. Biferale, S. Succi, K. Sugiyama, F. Toschi, Generalized lattice Boltzmann method with multirange pseudopotential, Phys. Rev. E - Stat. Nonlinear, Soft Matter Phys. 75 (2007) 1–13, https://doi.org/10.1103/PhysRevE.75.026702.

[60] P. Yuan, L. Schaefer, Equations of state in a lattice Boltzmann model, Phys. Fluids. 18 (2006), https://doi.org/10.1063/1.2187070.

[61] Q. Li, P. Zhou, H.J. Yan, Pinning-Depinning mechanism of the contact line during evaporation on chemically patterned surfaces: a lattice Boltzmann study, Langmuir. 32 (2016) 9389–9396, https://doi.org/10.1021/acs.langmuir.6b01490.

[62] M. Wang, N. Pan, Predictions of effective physical properties of complex multiphase materials, Mater. Sci. Eng. R Reports. 63 (2008) 1–30, https://doi.org/10.1016/j.mser.2008.07.001.